# A Novel 3D Visualization Method in Mice Identifies the Periportal Lamellar Complex (PLC) as a Key Regulator of Hepatic Ductal and Neuronal Branching Morphogenesis

Tongtong Xu[1#], Fujun Cao[1#],Ruihan Zhou[1#], Qin Chen[2],Jian Zhong[3],Yulin Wang[1],Chaoxin Xiao[1],Banglei Yin[1],Chong Chen[1], Chengjian Zhao1*

#These authors contributed equally: Tongtong Xu, Fujun Cao,Ruihan Zhou

*Correspondence: chjianzhao@scu.edu.cn

[1] State Key Laboratory of Biotherapy, West China Hospital, Sichuan University, and Collaborative Innovation Center for Biotherapy, Sichuan, China

[2] Chengdu Minghong Tiancheng Technology Co., Ltd.

[3] Peking University Chengdu Academy for Advanced Interdisplinary Biotechnologies Chengdu

Graphical abstract

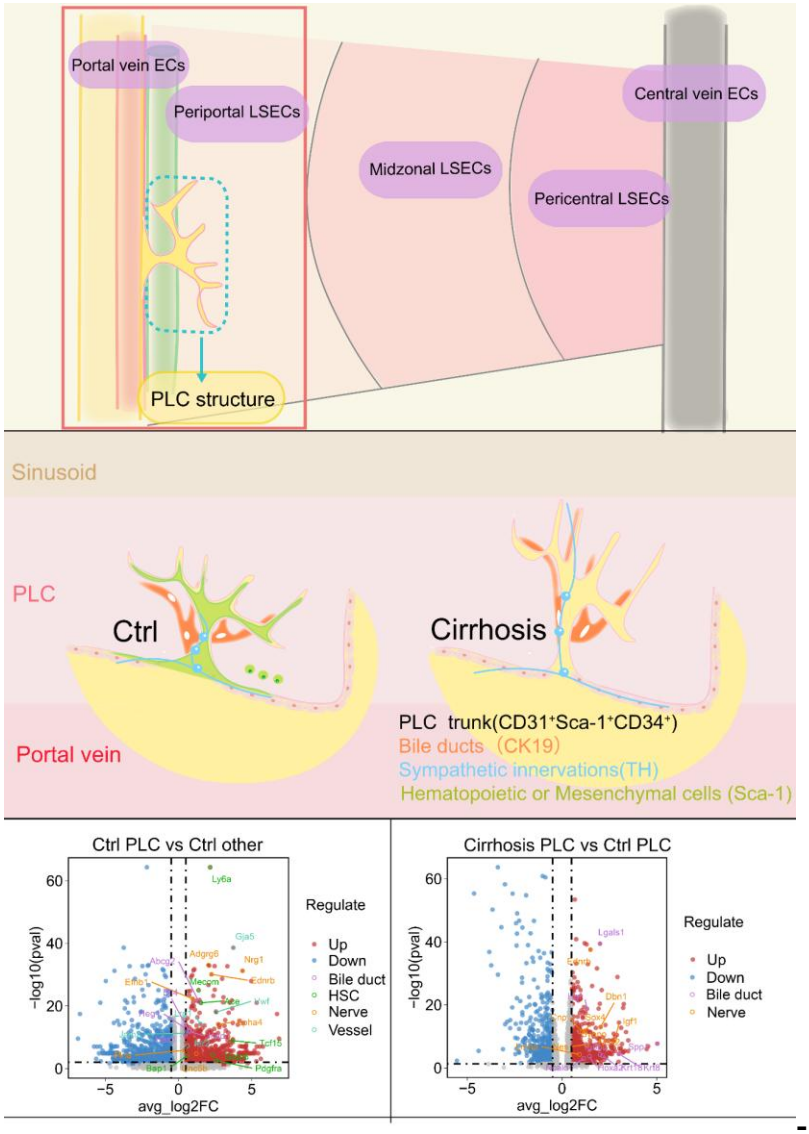


## Summary


The liver's microenvironment consists of interconnected vascular, biliary, and neural networks that regulate homeostasis and disease progression. However, the lack of high-resolution 3D visualization hinders our understanding of their interactions in health and pathology.

In this study, we developed a high-resolution multiplex 3D imaging method integrating multicolor metallic compound nanoparticle (MCNP) perfusion and

optimized CUBIC tissue clearing, enabling simultaneous 3D visualization of the portal vein, hepatic artery, bile ducts, and central vein spatial networks in mouse liver.

Using this approach, we identified a novel perivascular structure, the Periportal Lamellar Complex (PLC), regularly distributed along the portal vein axis between its endothelium and the periportal lobule sinusoid. The PLC contains a unique population of $CD34^+Sca\text{-}1^+$ dual-positive endothelial cells with a distinct gene expression profile, potentially linked to bile acid transport, biliary epithelial cell proliferation, and neural development.

Under normal physiological conditions, the PLC colocalizes with terminal bile duct branches and sympathetic nerve fibers. During liver fibrosis progression, the PLC dynamically extends into liver lobules alongside advancing fibrosis, acting as a scaffold guiding the migration of bile ducts and nerve fibers into the hepatic parenchyma. Differential gene expression and GO enrichment analyses further revealed neurodevelopmental and axon guidance pathway enrichment in the $CD34^+Sca\text{-}1^+$ endothelial population of PLC during fibrosis.

Collectively, these findings establish the PLC as a critical structural and functional hub integrating hepatic vascular, biliary, and neural systems to regulate liver function. This study advances our understanding of liver biology and offers potential therapeutic targets for liver diseases.

## INTRODUCTION

The liver performs diverse physiological functions including nutrient metabolism, detoxification, bile secretion, and immune regulation, all of which rely on its unique microanatomy — the hepatic lobule, the smallest structural and functional unit [1-5]. To sustain the efficient operation of the vast number of hepatic lobules distributed throughout the parenchyma, the liver has evolved the most complex and densely n organized vascular network in the body, consisting primarily of the portal vein system, central vein system, hepatic artery system, biliary system, and intrahepatic autonomic nerve network [6, 7]. Together, these systems form a multicompartmental 3D network, integrating blood transport, bile drainage, and neuroimmune regulation essential for maintaining the hepatic microenvironment. Despite their distinct physiological

functions, these systems are closely interconnected, coordinating with one another to support metabolic, immune, and regenerative processes within each lobule [7]. While macroscopic hepatic vascular patterns and metabolic zonation have been described [8, 9]. how these networks interact with countless microscale, spatially heterogeneous lobules remains poorly understood.

Traditional two-dimensional (2D) histological analysis, while offering high spatial resolution, has long been regarded as the gold standard for morphological studies [10, 11]. However, it presents notable limitations when applied to the investigation of complex three-dimensional (3D) vascular systems. On one hand, single-section analyses cannot restore the full 3D connectivity of vascular structures, while serial section reconstruction is prone to alignment errors and remains inadequate for resolving the interactions among multiple ductal systems. Therefore, achieving 3D-level visualization of multiple intrahepatic vascular systems is essential for studying their dynamic interactions during liver development, homeostasis, and disease progression. Conventional imaging modalities such as ultrasound, micro-computed tomography (Micro-CT), and magnetic resonance imaging (MRI) are widely applied in both experimental animal studies and clinical practice. Although these techniques can capture gross pathological alterations in the hepatic vasculature, they lack the spatial resolution required to resolve micrometer-scale structures. X-ray phase-contrast computed tomography (PCCT), recently developed for liver microvascular imaging, has achieved contrast-agent-free microvasculature visualization in rat livers[12] . However, its contrast sensitivity remains insufficient for resolving subcellular structures. Similarly, the DUCT technique successfully reconstructed a 3D portal vein–bile duct network in the mouse liver via dual-color resin casting, but was limited by its inability to resolve luminal structures smaller than 5 μm [11]. To fully understand how multiple hepatic ductal systems maintain their intricate terminal 3D interactions — such as portal vein–hepatic artery blood flow coupling, bile duct–vessel countercurrent exchange, and nerve–vessel signaling — and how these systems collectively coordinate with liver lobules, a more effective multicolor, high-resolution 3D imaging strategy is urgently needed. Nevertheless, integrating such approaches for the liver remains challenging for several reasons. First, the hepatic vasculature is structurally complex, featuring ultra-

dense vascular distributions (with hepatic sinusoids occupying 10–15% of liver volume) and multilevel, intertwined arrangements (arterial branches encircling portal vein branches, and bile ducts running parallel to blood vessels). Imaging must therefore achieve submicron spatial resolution (≤1 μm) while maintaining millimeter-scale tissue penetration depth[8, 13].Second, the liver's tissue-specific properties significantly interfere with imaging. Endogenous pigments (such as bilirubin and lipofuscin) and strong autofluorescent components (such as collagen and NADPH/FAD) severely impair tissue-clearing efficiency and degrade fluorescence signal quality, resulting in a low signal-to-noise ratio (SNR) in traditional clearing–staining–imaging workflows[14-16].Third, multiple intrahepatic systems — including blood vessels, bile ducts, nerves, lymphatics, and immune cell networks — are densely interwoven and functionally interdependent. However, there is currently a lack of efficient 3D multi-target labeling strategies capable of simultaneously visualizing these systems in both their hierarchical macroscopic structures and their fine terminal interactions. In summary, the liver's unique structural complexity and tissue-specific properties impose significant constraints on the performance of existing clearing techniques (such as CLARITY and iDISCO) and labeling protocols (such as immunohistochemistry and immunofluorescence) in 3D imaging applications, limiting imaging depth, resolution, and SNR[14, 17]. Compared to organs such as the brain and kidney, the application of 3D, high-resolution, multicolor imaging in the liver remains markedly underdeveloped. Given these limitations, the development of liver-adapted, high-fidelity clearing strategies, deep multi-target labeling systems, and compatible 3D imaging platforms has become an urgent priority and a key technical breakthrough needed to advance both physiological and pathophysiological studies of the liver.

An ideal three-dimensional (3D) visualization technique for the liver should enable clear delineation of the hierarchical architecture and structural alterations of the vascular systems at a macroscopic level, while simultaneously allowing the observation of terminal vascular structures coordinating with liver lobules at a single-cell resolution. Considering the unique anatomical and cellular characteristics of the liver, our research team has developed an advanced 3D visualization strategy tailored for the hepatic multi-ductal system, building upon existing imaging technologies. The

core innovations of this strategy include:(1) Establishment of an efficient liver clearing protocol (liver-CUBIC): By systematically optimizing sample processing procedures and reagent compositions within the CUBIC tissue clearing framework, we achieved a 63.89% improvement in clearing efficiency and a 20.12% increase in tissue transparency.(2) Selection and application of multicolor metal compound nanoparticles (MCNPs): These nanoparticles exhibit excellent water resistance and compatibility with the Liver-CUBIC system. Their multicolor properties enable stable, simultaneous 3D labeling of the portal vein, hepatic artery, bile ducts, and central vein in mouse livers. Moreover, the MCNP series possesses unique excitation/emission spectra, making them suitable for multimodal imaging applications including brightfield, extended depth of field (EDF), and fluorescence microscopy. Their high spatial resolution supports the visualization of fine vascular terminal branches and subcellular structures.(3) Development of a multimodal immunolabeling system: This 3D visualization strategy is compatible with both DAB chromogenic and TSA-based multiplex immunofluorescence staining, enabling simultaneous labeling of various cell types and molecular antigens alongside vascular system visualization. This allows for the generation of high signal-to-noise ratio, multi-target, subcellular-resolution 3D structural maps of the liver. In summary, this newly established 3D visualization platform for hepatic multi-ductal systems provides both macroscopic and microscopic insights, offering a powerful tool for investigating the spatial organization, functional coordination, and pathological remodeling mechanisms of the liver microenvironment.

Based on this platform, we successfully applied the proposed strategy to investigate the microanatomical architecture of the hepatic vascular system in mice, with a particular focus on elucidating how the complex intraparenchymal vascular networks are spatially organized and coordinate with liver lobule units at single-cell resolution. Through multimodal microscopic visualization, multicolor antigen-specific labeling, and targeted gene expression analysis, we identified a previously unrecognized functional structure termed the Periportal Lamellar Complex (PLC). This novel structure is distributed periodically along the portal vein axis and is closely associated with terminal bile duct branches and autonomic nerve plexuses, forming a specialized spatial interaction unit. Single-cell transcriptomic analysis combined with multiplex 3D

immunostaining confirmed that the PLC possesses distinct spatial localization, morphological features, and molecular marker profiles within the murine liver. Its unique gene expression signatures and intimate interactions with multiple terminal vascular branches suggest a cooperative mechanism underlying hepatic microanatomical organization.

This discovery not only validates the superior capability of our multi-ductal 3D visualization platform in resolving microscale hepatic vascular interactions but also provides a technical foundation for establishing a new paradigm in hepatic vascular research. By enabling full-scale visualization from the organ to the vascular network and down to the single-cell level, this platform offers a powerful methodological tool for uncovering regulatory mechanisms of hepatic physiology and pathological remodeling.

**$H_2O_2$-Enhanced CUBIC Clearing Coupled with Multicolor Nanoprobes for High-Resolution 3D Mapping of Liver Ductal -Vascular network**

The CUBIC (Clear, Unobstructed Brain/Body Imaging Cocktails and Computational analysis) technique has been widely applied in the tissue clearing and 3D imaging of organs such as the brain, kidney, and heart due to its excellent compatibility with various fluorescent dyes and immunolabeling protocols[15, 16] . However, the application of CUBIC in liver tissue remains challenging because of the liver's high heme content and densely packed cellular architecture, which leads to pronounced light scattering and markedly limits the clearing efficacy. In addition, the conventional CUBIC protocol requires up to 9 days for liver tissue processing, severely restricting experimental throughput (Figure 1A, red schematic).To address these limitations, Laura M. Molina et al. incorporated a hydrogen peroxide ($H_2O_2$) bleaching step into the CLARITY protocol, improving liver transparency but failing to reduce the processing time; clearing efficiency also remained suboptimal [14] In this study, we developed an optimized clearing strategy termed Liver-CUBIC, featuring two key modifications:(1) Integration of an $H_2O_2$-CUBIC hybrid system, incorporating an $H_2O_2$ bleaching step into the CUBIC workflow. This dual-action mechanism effectively removes pigments such as heme and lipofuscin through oxidative reactions, while partially clearing lipid components to reduce light

scattering.(2) Optimization of urea concentration, increasing from 25% to 40%, enhancing protein denaturation to minimize light scattering and improve tissue permeability, thus promoting more uniform reagent distribution. Experimental results confirmed that the Liver-CUBIC protocol significantly improved liver clearing efficiency (Figure S1A). Specifically, initial PBS/PFA perfusion efficiently removed residual heme (Figure S1A, panel 2); subsequent $H_2O_2$ bleaching eliminated pigment deposits (Figure S1A, panel 3); and final 40% urea treatment achieved refractive index homogenization (Figure S1A, panel 4).Using this optimized protocol, the total clearing time was reduced from 9 days with conventional CUBIC (25% urea, Figure 1A, red schematic) to 3.25 days with 40% urea + $H_2O_2$ treatment (Figure 1A, green schematic), representing a 63.89% increase in efficiency. Importantly, no significant tissue expansion was observed following Liver-CUBIC treatment (Figures 1B and 1D).Transmittance measurements revealed that the Liver-CUBIC protocol (40% urea + $H_2O_2$) markedly outperformed conventional CUBIC, with an average transmittance improvement of 20.12% ($P < 0.0001$; 95% CI: 19.14–21.09) (Figure 1E). Additionally, in 1 mm-thick liver sections, the clearing time was reduced to just 20 minutes (Figure S1B), while real-time imaging demonstrated complete clearing of 200 μm-thick slices within 60 seconds (Figure S1C; Supplementary Video 1), fully meeting the demands for rapid live imaging.

Metal compound nanoparticles (MCNPs) exhibit excellent brightness, tunable multicolor properties, and strong resistance to $H_2O_2$ bleaching, maintaining color stability even after Liver-CUBIC clearing. Utilizing four distinct MCNP colors — pink, green, black, and yellow — we developed a four-channel vascular labeling strategy (Figures 1F and S1D). The hepatic artery was perfused with yellow MCNPs via the left ventricle, bile ducts were retrogradely injected with green MCNPs through the extrahepatic duct, portal veins were directly filled with pink MCNPs, and central veins were labeled using black MCNPs via the inferior vena cava Using this method, simultaneous four-color labeling of the intrahepatic ductal-vascular system can be achieved (Figures S1E–S1G), while single- or dual-color labeling allows for higher-resolution visualization of fine microscale structures. High-resolution 3D imaging revealed that MCNP-Green-labeled large intrahepatic bile ducts exhibit a one-to-one parallel topology with adjacent portal vein branches. At the periphery, the terminal

biliary network forms a classic three-dimensional plexus, characterized by helical configurations and polygonal extensions projecting into the hepatic lobules (Figure 1G).Meanwhile, MCNP-Pink-labeled portal veins displayed a typical tree-like branching pattern in the central regions of hepatic lobes, but in the marginal areas, they formed an unusually dense, radial micro-branching pattern (Figure 1H). Notably, the terminal micro-branches of the portal vein appeared not only around secondary branches but also intermittently along the main trunks, challenging the conventional notion of strictly hierarchical vascular bifurcation. For MCNP-Black-labeled central veins, imaging revealed sparse, circular or oval fenestrae measuring 50–100 nm in diameter distributed across the surface of the central vein trunks (Figure 1I). Previous scanning electron microscopy studies have described similar structures, which are thought to facilitate the return of hepatocyte-synthesized metabolic products (such as lipoproteins and cytokines) into the circulation, assist immune cell trafficking from the liver to the systemic circulation, and help maintain hepatic sinusoid–interstitium osmotic pressure balance[18]. Additionally, dual-label imaging using MCNP-Pink and MCNP-Green demonstrated that the hepatic artery runs parallel to the portal vein trunk, with the hepatic artery displaying a notably smaller diameter compared to its adjacent portal vein. At the periphery, hepatic arterial branches formed a three-dimensional entwined network that closely contacted the portal vein micro-branches (Figure 1J).

In summary, combining liver-CUBIC with MCNPs enabled highly efficient, simultaneous mapping of intrahepatic bile ducts, portal veins, central veins, and hepatic arteries in mice at cellular resolution, revealing their spatial organization and topological relationships.

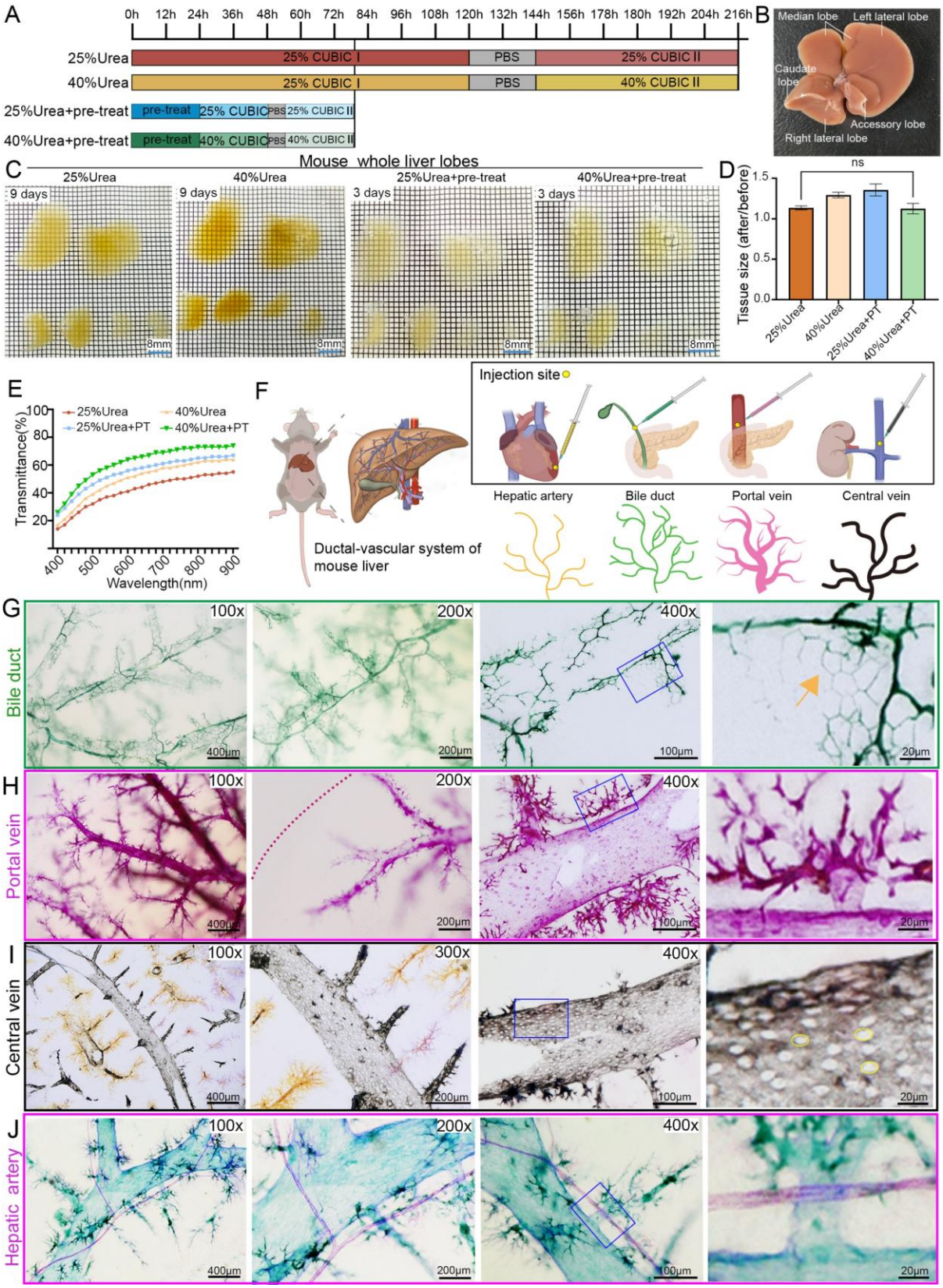


**Figure1.$H_2O_2$-Enhanced CUBIC Clearing Coupled with Multicolor Nanoprobes for High-Resolution Mapping of Liver Vasculature.**

(A) Comparison of processing times for four different liver clearing protocols: conventional CUBIC (25% urea, red), high-concentration urea (40% urea, yellow), oxidation treatment alone (25% urea + 4.5% $H_2O_2$, blue), and the optimized Liver-CUBIC (40% urea + 4.5% $H_2O_2$, green). The optimized Liver-CUBIC protocol significantly reduced clearing time (n = 6 per group).

(B) Schematic illustration of mouse liver lobes, defining left lateral lobe, left medial lobe, right medial lobe, right lateral lobe, caudate lobe, and quadrate lobe according to reference [19] .
(C)Brightfield images of whole mouse livers (8–9 weeks old, male) after processing with the four clearing protocols. Grid size: 1.6 mm × 1.6 mm. Scale bar: 8 mm.
(D) Quantitative analysis of tissue volume changes following each clearing protocol (n = 6 per group). No statistically significant difference was observed between the 25% urea group and the 40% urea + $H_2O_2$ group. Statistical test: unpaired two-tailed t-test. PT: pre-treatment.
(E) Transmission spectra (400–900 nm) of 1 mm-thick mouse liver samples after each clearing protocol (n = 5 per group).
(F) Schematic diagram of the four-channel ductal-vascular labeling strategy: yellow MCNPs injected via the left ventricle to label hepatic arteries, green MCNPs via retrograde common bile duct injection to label biliary ducts, pink MCNPs via the portal vein trunk to label portal veins, and black MCNPs via the inferior vena cava to label hepatic veins.
(G) Three-dimensional fine structures of the biliary tree in the central and peripheral regions of the mouse liver, labeled with MCNP-Green. Images are shown at magnifications of 100×, 200×, and 400×. The rightmost panel presents a high-magnification view of the area outlined by the blue box. Scale bars: 400 μm, 200 μm, 100 μm, and 20 μm. The arrow indicates the terminal ductal structures with a polygonal shape.
(H)Three-dimensional reconstruction of the portal venous system labeled with MCNP-Pink, showing branching features in central and peripheral zones. Images captured at 100×, 200×, and 400× magnifications; the rightmost image is a higher-magnification view of the blue-boxed region. Scale bars: 400 μm, 200 μm, 100 μm, and 20 μm.
(I) Three-dimensional structural details of the central vein labeled with MCNP-Black. Images captured at 100×, 300×, and 400× magnifications; the rightmost image is a higher-magnification view of the blue-boxed region. Scale bars: 400 μm, 200 μm, 100 μm, and 20 μm.
(J) Three-dimensional structural details of the hepatic artery labeled with MCNP-Pink. Images captured at 100×, 200×, and 400× magnifications; the rightmost image is a higher-magnification view of the blue-boxed region. Scale bars: 400 μm, 200 μm, 100 μm, and 20 μm.

**The Periportal Lamellar Complex (PLC) Serves as a Low-Permeability Gateway Bridging Portal Veins to Hepatic Lobules**

In this study, scanning electron microscopy revealed that MCNP dye is a nanoparticle-based labeling agent with a diameter of approximately 100 nm (Figure 2A). We employed a dual-channel vascular labeling strategy to simultaneously visualize the portal vein and hepatic artery systems in the mouse liver. Specifically, MCNP-Green was employed to label the portal venous system by injection from portal vein, while MCNP-Pink marked the hepatic arterial system by injection extrahepatic duct(Figure 2B).

Extended depth-of-field imaging revealed that MCNP-Green specifically labels a distinct vascular structural unit located in the adventitial layer of the portal vein trunk, which we designate as the Periportal Lamellar Complex (PLC) (Figures 2C and 2D, orange arrows). Morphologically, this structure consists of fine vascular branches distributed along the surface of the portal vein trunk. Its base is anchored to the portal vein, and it radiates outward in a lobular pattern centered on the portal vein, giving rise to multiple terminal branches that directly connect to the liver sinusoids (Figure 2C). The PLC structures align in a serial arrangement along the portal vein trunk (Figure 2D).

Further validation by confocal fluorescence imaging confirmed that following portal vein perfusion with MCNP-Green, fluorescence signals are highly enriched within the PLC. Quantitative analysis showed that the fluorescence intensity within the PLC was significantly higher than that observed in the portal vein lumen and liver sinusoid regions, with minimal dye diffusion at the PLC periphery, indicating predominant localization within the main PLC structure (Figures 2G–2J). In contrast, MCNP-Pink signals, introduced via hepatic artery perfusion, predominantly localized within the PLC and its margins without crossing into adjacent PLC units. Due to differences in perfusion pathways, the pink dye demonstrated a greater tendency to extend from the PLC towards the lobular parenchyma compared to the green dye. This phenomenon likely reflects the relatively low permeability of the PLC region: green nanoparticles delivered through the portal vein are largely retained within the low-permeability PLC core, with limited peripheral diffusion, whereas the arterial pink dye, influenced by the pressure and flow characteristics of the hepatic artery system, effectively labels the peripheral PLC structures (Figures 2G–2J).

Using the Extended Depth-of-Field Multimodal Imaging System, we quantitatively analyzed the distribution of PLC structures in relation to portal vein diameter and anatomical location. By defining classical hexagonal hepatic lobule units through the primary portal vein trunk containing PLC structures and its two adjacent secondary branches (Figure 2H), quantitative analysis revealed that the length of the primary portal vein trunk ranged from 269.85 μm to 1513.67 μm (n = 19), with a median length of 769.89 μm (IQR: 593.67 μm–987.77 μm). The number of PLC structures per trunk ranged from 1 to 4, with 68.42% (13/19) of portal veins containing two PLCs (Figure S2A). Notably, neither the number nor the area of PLCs showed significant correlation with the length of the portal vein trunk (Figures S2A and S2B), indicating that morphological parameters alone (such as trunk length) may be insufficient to define hepatic lobular units, especially given the substantial differences in blood transport capacity among portal veins of varying diameters. The diameters of the primary portal veins bearing PLC structures ranged from 63.45 μm to 321.42 μm, and PLC area showed a significant positive correlation with portal vein diameter (Figure 2L), whereas PLC number did not correlate with diameter (Figure S2C). This diameter–area relationship may reflect a

functional adaptation of the portal venous system in metabolically active liver regions: larger-diameter portal veins accommodate higher blood flow and consequently experience greater shear stress on the vessel wall. The formation of PLC structures in the adventitial layer may participate in local blood flow regulation, maintenance of microenvironmental homeostasis, and vascular–stem cell interactions.

These findings suggest that the Periportal Lamellar Complex (PLC) is not only a morphologically and spatially distinct, low-permeability vascular unit surrounding the portal vein, but also likely serves as a critical nexus connecting the portal vein, hepatic artery, and liver sinusoids. Thus, the PLC constitutes a key node within the interactive vascular network of the mouse liver.

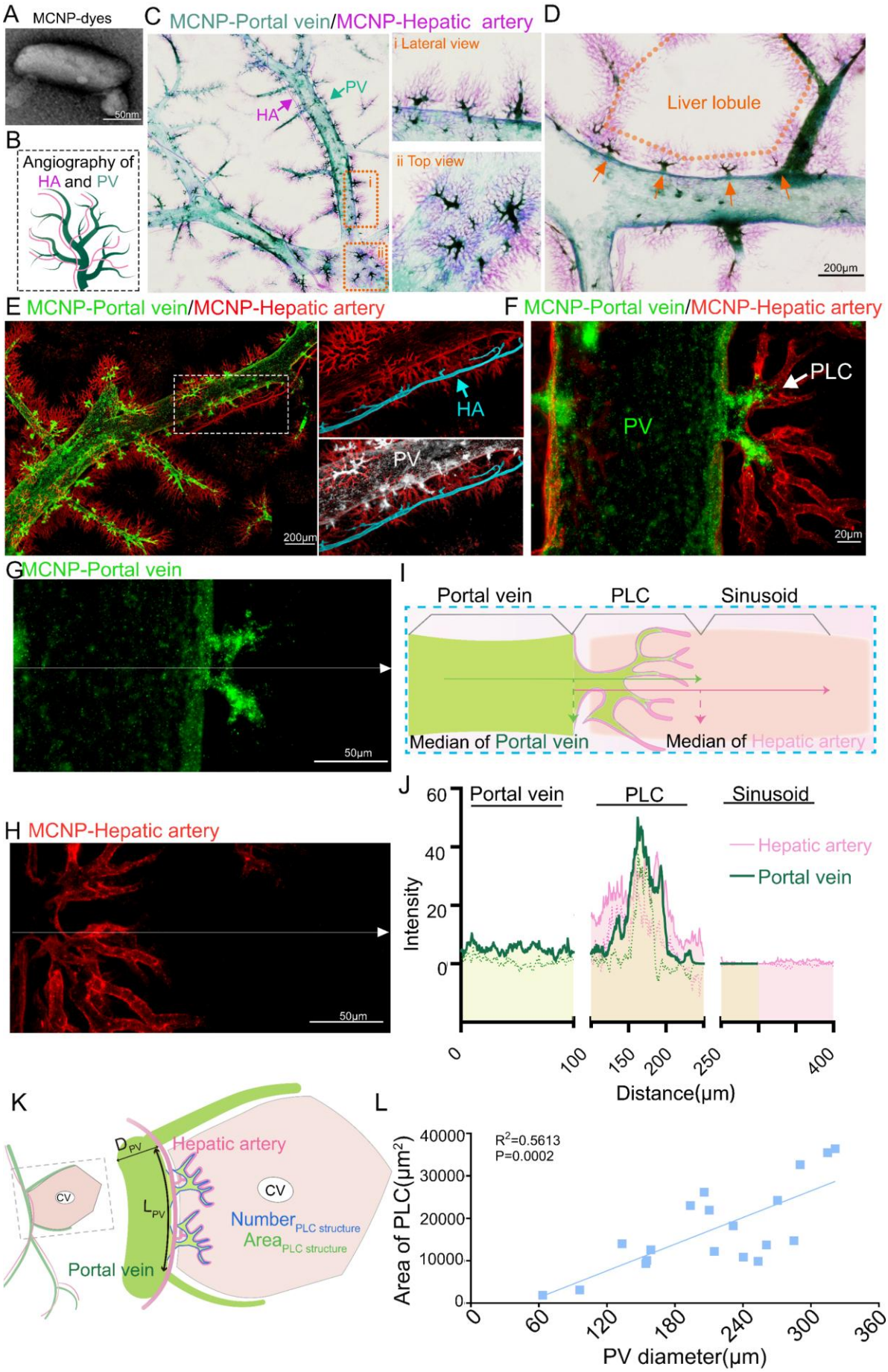
A
MCNP-dyes
50nm
B
Angiography of
HA and PV
C
MCNP-Portal vein/MCNP-Hepatic artery
PV
HA
i
ii
i Lateral view
ii Top view
D
Liver lobule
200μm
E
MCNP-Portal vein/MCNP-Hepatic artery
HA
PV
200μm
F
MCNP-Portal vein/MCNP-Hepatic artery
PLC
PV
20μm
G
MCNP-Portal vein
50μm
H
MCNP-Hepatic artery
50μm
I
Portal vein
PLC
Sinusoid
Median of Portal vein
Median of Hepatic artery
J
Portal vein
PLC
Sinusoid
Hepatic artery
Portal vein
Intensity
60
40
20
0
0
100
150
200
250
400
Distance(μm)
K
CV
$D_{PV}$
$L_{PV}$
Hepatic artery
CV
Number PLC structure
Area PLC structure
Portal vein
L
$R^2$=0.5613
P=0.0002
Area of PLC(μm²)
40000
30000
20000
10000
0
0
60
120
180
240
300
360
PV diameter(μm)

**Figure 2. The Periportal Lamellar Complex (PLC) Serves as a Low-Permeability Gateway Bridging Portal Veins to Hepatic Lobules**

(A) Scanning electron microscopy revealed that the Metal Compound Nanoparticles (MCNP) dyes consisted of aggregates of particles approximately 100 nm in length.

(B)Dual-channel vascular typing labeling scheme (Dual-channel NanoFluor™). hepatic arteries labeled with pink fluorescent nanoparticlesportal veins labeled with green fluorescent nanoparticles.

(C) Extended depth-of-field imaging (tissue thickness: 200 μm) reveals fine three-dimensional structural details of the hepatic artery and portal vein. The right panel shows magnified lateral and top views of the orange-boxed region, highlighting dense terminal branches and the close spatial proximity between the two vascular systems. Green arrows indicate portal veins, and pink arrows indicate hepatic arteries.

(D) Magnified image showing periodic alignment of PLC structures (orange arrows) along the adventitial layer of the portal vein trunk (green) in the direction of vascular flow. Orange dashed lines delineate the boundaries of a classical hepatic lobule. Scale bar: 200 μm.

(E) Three-dimensional confocal imaging of hepatic arteries (pink dye, excitation/emission: 561/640 nm) and portal veins (green dye, excitation/emission: 495/519 nm). The right panel presents a high-resolution view with hepatic arteries rendered in blue and the portal vein surface filled in white; arrows indicate points of interaction between PLC structures and hepatic arteries. Scale bar: 200 μm.

(F) High-magnification confocal imaging further depicting micro-branches of portal veins and hepatic arteries, with terminal branches intertwining in a coiled distribution. Scale bar: 20 μm.

(G, H) Single-channel confocal images showing the distribution of MCNP-Green-labeled portal veins (G) and MCNP-Pink-labeled hepatic arteries (H) within PLC regions. White arrows indicate the paths of fluorescence intensity profile measurements, with arrowheads denoting the direction of line scans. Scale bar: 50 μm.

(I) Schematic illustration of fluorescence intensity profile measurements across PLC structures. The midpoint of the portal vein (green) intensity profile corresponds to the junction between the PLC and the outer wall of the portal vein, while the midpoint of the hepatic artery (pink) intensity profile aligns with the terminal edge of the PLC adjacent to liver sinusoids. Arrows indicate scan directions.

(G) Fluorescence intensity profile plots. The X-axis represents the scan distance (0–400 μm), and the Y-axis represents fluorescence intensity. Both portal vein (green) and hepatic artery (pink) signals showed significant increases within the PLC region. The regions were defined as follows: 0–100 μm, portal vein region; 100–250 μm, PLC region; 250–400 μm, liver sinusoid region (n = 5 per group).

(K) Analytical workflow for characterizing PLC structures: the primary portal vein trunk carrying PLC structures was selected as the reference axis for hepatic lobule boundaries, combined with its two adjacent secondary branches to define a classical hexagonal lobule computational unit. The diameter of the primary portal vein trunk (dPV) and the area of PLC structures were quantified using the extended depth-of-field imaging system.

(L) Distribution of PLC areas along primary portal vein trunks with diameters ranging from 63.45 to 321.42 μm. Each value represents the PLC area associated with a portal vein of corresponding diameter (n = 19).

**Spatial Juxtaposition of the Periportal Lamellar Complex with Canals of Hering at the Portal Venous Interface**

To further investigate the potential relationship between the PLC and bile delivery regulation within the hepatic lobule, we employed a dual-channel vascular labeling strategy to simultaneously visualize the mouse liver portal vein and bile duct systems.

We combined MCNP-Pink labeling of the portal vein and its associated PLC structures with three-dimensional DAB immunohistochemical staining for CK19 to visualize the bile duct epithelial architecture. Extended depth-of-field three-dimensional bright-field imaging revealed a strict 1:1 anatomical association between the primary portal vein trunk (diameter 280 ± 32 μm) and the first-order bile duct (diameter 69 ± 8 μm) (Figures 3A and S3A).From multiview imaging showed that second-order bile ducts are distributed along the portal vein trunk and branch directionally toward the PLC. Their terminal portions, namely the canals of Hering, form the distal bile duct network responsible for bile collection, and are located at the interface between hepatic lobules, rather than being evenly distributed around the portal vein. Instead, these terminal ducts are specifically concentrated within the PLC surrounding the portal vein, displaying marked spatial colocalization (Figure 3A). This finding suggests a potential anatomical spatial association between the terminal canals of Hering and the periportal PLC structures. Furthermore, based on MCNP-Green labeling of the biliary tract, combined with 3D DAB-CK19 staining, both extended depth-of-field bright-field imaging and 3D confocal fluorescence imaging consistently confirmed that the terminal regions of the biliary network—responsible for collecting bile from the hepatic parenchyma—are primarily located adjacent to the PLC (Figures 3B, 3C, and S3B).

To delineate the microscopic architecture underlying bile flow from the hepatic parenchyma into the bile duct network, we employed three-dimensional TSA-based multiplex immunofluorescence to simultaneously label the tight junction protein ZO1, the hepatocyte nuclear marker HNF4A, and the bile duct epithelial marker CK19 (Figure 3D). Three-dimensional confocal imaging demonstrated that bile canaliculi on the hepatocyte surface formed polygonal networks demarcated by ZO1, while terminal bile duct epithelial cells also organized into luminal structures via ZO1, arranged in either

single- or multicellular rings, thereby establishing an interface between the canalicular network and the bile duct system. However, detailed morphological analysis suggested that this connection does not occur directly between the bile canaliculi and the terminal bile duct epithelial cells. Instead, bile duct epithelial cells at the terminal ducts extended partially along the canalicular network without directly participating in the formation of the bile duct lumen. This finding indicates that these cells may remain in an immature state or possess alternative stem/progenitor cell-like properties [20, 21]. To further verify the precise interface between the terminal bile ducts and the bile canalicular network, we performed retrograde perfusion of MCNP-Green dye through the common bile duct while progressively increasing the perfusion pressure. When the dye pressure exceeded a defined threshold, dye leakage was observed (Figures 3E-3G, and S3C). Dual-channel three-dimensional confocal imaging combined with CK19 immunostaining revealed that the sites of dye leakage did not coincide with the CK19-positive terminal bile duct epithelium, but instead were predominantly localized within regions adjacent to the PLC structures (Figures 3E-3G, and S3C).This observation further supports our earlier hypothesis: first-order bile ducts distribute along the portal vein trunk, secondary bile ducts branch directionally toward the PLC regions, and terminal bile duct branches converge spatially adjacent to the PLC, where they collect bile drained from the hepatic lobules. These results suggest that the PLC may serve not only as a spatial positional cue guiding bile duct growth and branching but also as a regulatory node involved in coordinating bile drainage from the hepatic lobule into the biliary network.

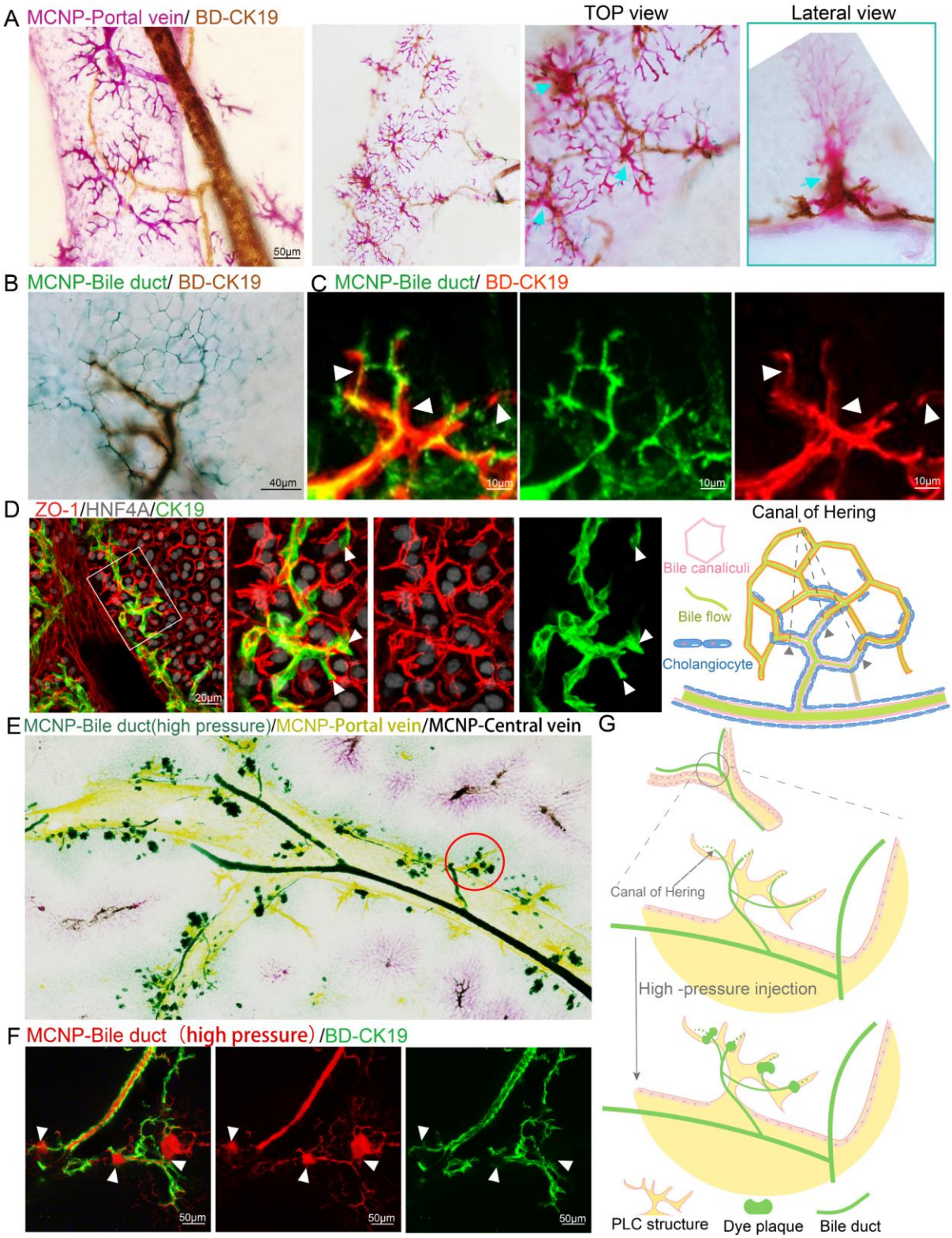


**Figure 3. Spatial Juxtaposition of the Periportal Lamellar Complex with Canals of Hering at the Portal Venous Interface**

(A) MCNP-Pink labeling of portal veins combined with three-dimensional DAB immunohistochemistry for CK19 (brown) to visualize bile duct epithelial cells. Top and lateral views highlight the PLC–bile duct interaction sites (cyan arrows). Scale bar: 50 μm.

(B) MCNP-Green labeling of bile ducts combined with three-dimensional DAB immunohistochemistry for CK19

(brown). Scale bar: 40 μm.

(C) MCNP-Green labeling of bile ducts combined with three-dimensional TSA immunofluorescence for CK19 (red), displaying detailed structures at the interface between dye-labeled ducts and immunostained bile duct terminals. The arrows indicate the terminal structures of the bile ducts. Scale bar: 10 μm.

(D) Three-dimensional TSA multiplex immunofluorescence staining for ZO-1 (red, marking bile canaliculi networks), HNF4α (gray, marking hepatocyte nuclei), and CK19 (green, marking bile ducts). Scale bar: 20 μm. The right panel illustrates the spatial relationship between ZO-1-labeled bile canaliculi and CK19-labeled bile duct terminals, with arrows indicating the terminal positions of bile ducts.

(E) Extended depth-of-field imaging of the whole liver showing high-pressure perfusion of green fluorescent nanoparticles into the bile duct, yellow nanoparticles labeling the portal vein. Red circles indicate sites of green dye leakage localized to the PLC regions.

(F) High-pressure retrograde perfusion of red fluorescent nanoparticles into the bile duct, combined with three-dimensional TSA immunofluorescence for CK19 (green). Arrows indicate sites of dye leakage at the PLC region. Scale bar: 50 μm.

(G) Schematic diagram illustrating the leakage sites of bile duct-perfused dye following high-pressure injection. Green dashed boxes represent the positions of free bile duct terminal epithelial cells at leakage sites.

## Single-Cell Transcriptomics Identifies CD34$^+$Sca-1$^+$ as a Novel Endothelial Signature of the Periportal Lamellar Complex with Hematopoietic Niche Potential

To identify the transcriptional profiles of endothelial cells (ECs) of PLC, we re-analyzed publicly available single-cell RNA sequencing (scRNA-seq) data of liver endothelial cells isolated by fluorescence-activated cell sorting (FACS) from the livers of three healthy adult mice[22]. Unsupervised clustering identified a total of 10 distinct cell clusters (Figures 4A and 4B). Among these, several clusters contained contaminating non-endothelial cell populations expressing marker genes for hepatocytes, T cells, cholangiocytes, and macrophages (Figures 4A and 4B). These non-endothelial populations were excluded from subsequent analyses.Based on previously reported endothelial cell cluster-specific marker genes[23, 24], the remaining liver endothelial cells were classified into five distinct subpopulations: portal vein endothelial cells (Portal vein ECs), periportal liver sinusoidal endothelial cells (Periportal LSECs), midzonal liver sinusoidal endothelial cells (Midzonal LSECs), pericentral liver sinusoidal endothelial cells (Pericentral LSECs), and central vein endothelial cells (Central vein ECs) (Figures 4C, S4A and S4B).

The PLC structures are anatomically located within the transitional zone between portal vein ECs and periportal LSECs(Figure 4D). Most of the characteristic genes within this region exhibited a continuous gradient expression pattern, rather than displaying a distinct binary classification between portal vein ECs and Periportal LSECs. Based on this spatial continuum, we hypothesized that PLC endothelial cells might display a hybrid transcriptional signature, co-expressing marker genes derived from both adjacent endothelial populations (Figures 4C and 4D).To test this, we performed Venn diagram intersection analysis combined with differential gene expression screening, identifying a set of candidate genes potentially specific to PLC endothelial cells (Figure 4E). Subsequent validation by CmTSA staining confirmed that CD31, a pan-endothelial marker, reliably delineated the spatial boundaries of portal vein ECs, PLC endothelium, and periportal LSECs (Figure 4F). Notably, among the intersection genes, CD34 and Sca-1 (Ly6a) were co-expressed exclusively within the PLC structures surrounding the portal vein, but absent from both central vein ECs and midzonal LSECs (Figure 4F).Additionally, we examined the spatial distribution of other endothelial-associated markers in two-dimensional liver sections. CD36 was found to specifically label Periportal LSECs, while PDGFRβ was broadly expressed across multiple intrahepatic endothelial subtypes(Figure S4D). Comparative analysis indicated that the combination of $CD34^{+}Sca\text{-}1^{+}$ expression served as a superior marker set for identifying PLC endothelial cells.Based on this, we sorted $CD34^{+}Sca\text{-}1^{+}$ endothelial populations from the total liver endothelial cell pool (Figure 4G). Projection mapping analysis demonstrated that CD34 and Sca-1 were primarily distributed within Portal vein ECs, Periportal LSECs, and Midzonal LSECs (Figure S4C). Notably, CD34 and Sca-1 are also classical markers of mesenchymal stem cells and intrahepatic hematopoietic stem cells (HSCs), indicating potential stem/progenitor-like properties of PLC-associated endothelial cells[25-29]. Further analysis revealed that the $CD34^{+}Sca\text{-}1^{+}$ endothelial cell population, which marks the PLC structures, exhibited significantly upregulated expression of hematopoietic stem cell (HSC)-associated genes. Notably, *Mecom* — a critical transcriptional regulator essential for HSC self-renewal and highly expressed in human and approximately 60% of murine long-term HSCs[30, 31]— was prominently enriched within this population. In addition, *PDGFRα*, which together with Sca-1 serves as a classical marker for mesenchymal stem cell (MSC) isolation and may label

important mesenchymal progenitor cell populations known to promote hepatocyte differentiation via direct contact and growth factor secretion[32, 33], was also highly expressed (Figure 4H).Gene Ontology (GO) enrichment analysis further demonstrated that differentially expressed genes in the $CD34^+Sca\text{-}1^+$ population were significantly enriched in pathways associated with HSC proliferation, lineage differentiation, mesenchymal cell development, and hepatic cell fate determination (Figure 4I). These findings suggest that this unique endothelial subset possesses dual regulatory functions in both metabolic and hematopoietic modulation within the periportal region. Finally, three-dimensional structural reconstruction (Figure 4J) revealed that the main trunk of the PLC is composed of $CD34^+Sca\text{-}1^+CD31^+$ endothelial cells. In addition, a distinct "hematopoietic stem cell–vascular" niche unit formed by $CD34^+Sca\text{-}1^+$ double-positive cells was identified at the basal region of the PLC structure. This finding suggests that PLC endothelial cells not only regulate the periportal microcirculatory blood flow, but also establish a specialized microenvironment that supports periportal hematopoietic regulation, contributing to stem cell recruitment, vascular homeostasis, and tissue repair.

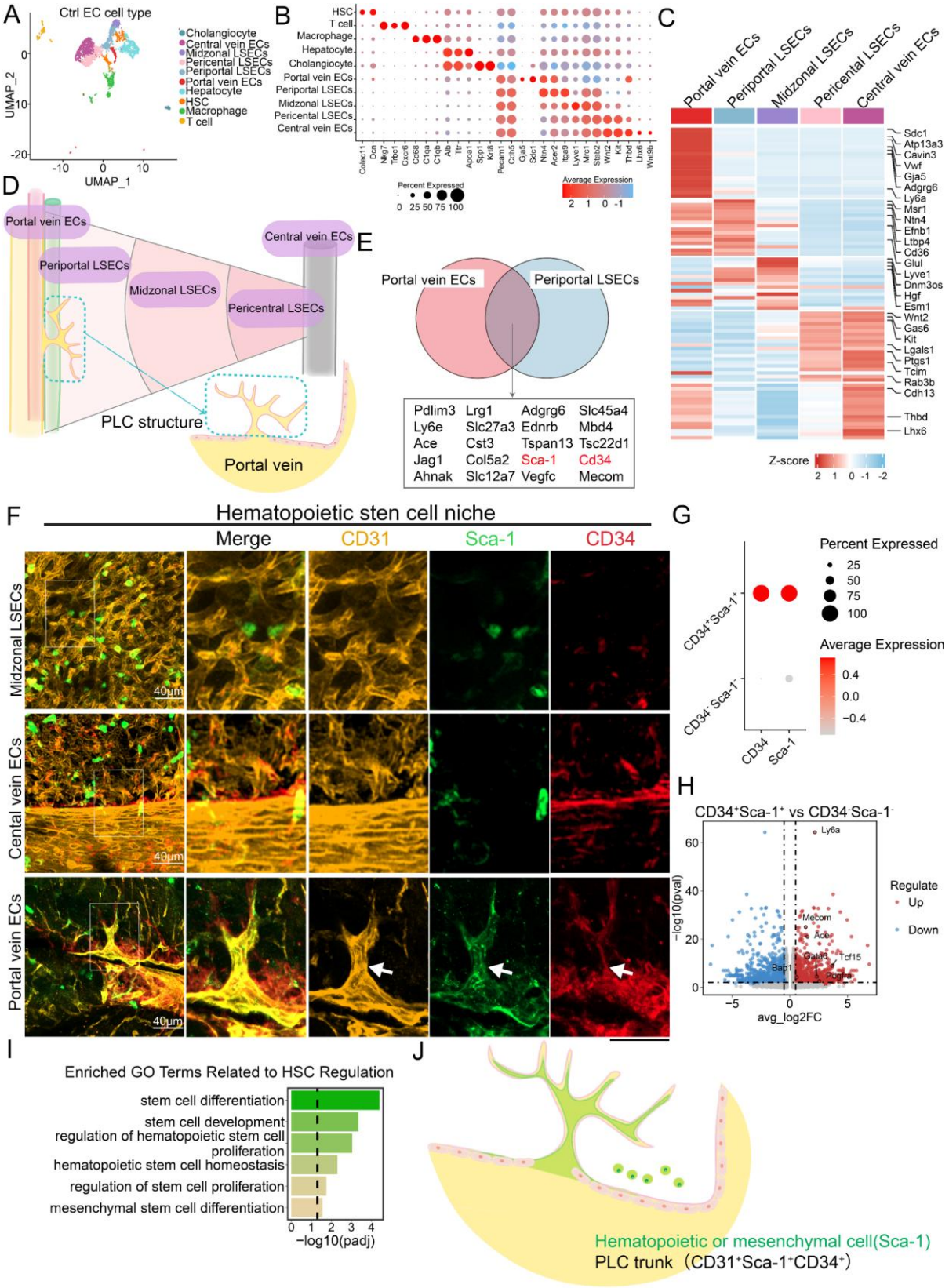


**Figure 4. Single-Cell Transcriptomics Identifies CD34⁺Sca-1⁺ as a Novel Endothelial Signature of the Periportal Lamellar Complex with Hematopoietic Niche Potential**

(A) UMAP projection of single-cell transcriptomes of liver endothelial cells from normal adult mice reveals 10 distinct cellular clusters. Each dot represents one cell.

(B) Heatmap showing expression profiles of representative genes across the 10 clusters, including hepatic stellate cells, T cells, macrophages, hepatocytes, cholangiocytes, prtal vein ECs, periportal LSECs, midzonal LSECs, pericentral LSECs, and central vein ECs . Marker genes were selected based on average cluster expression.
(C) Representative cluster-specific markers for five major liver endothelial subpopulations.
(D) Spatial schematic illustrating the anatomical position of the Periportal Lamellar Complex (PLC), located exclusively between the portal vein ECs and periportal LSECs.
(E) Venn diagram showing overlapping top 20 highly expressed genes between prtal vein ECs and periportal LSECs.
(F) Multiplex immunofluorescence images showing CD31 (yellow), Sca-1 (green), and CD34 (red) expression in distinct hepatic endothelial zones, including prtal vein ECs, midzonal LSECs, and central vein ECs. The PLC structure is demarcated by dashed white arrows. Scale bar: 40 μm.
(G) Gating strategy and classification of $CD34^+Sca\text{-}1^+$ double-positive versus double-negative endothelial subpopulations.
(H) Volcano plot illustrating differentially expressed hematopoietic-associated genes in $CD34^+Sca\text{-}1^+$ cells. The x-axis shows $\log_2$ fold-change ($\log_2$FC); the y-axis shows $-\log_{10}$ adjusted P value. Significantly upregulated genes are located in the upper right quadrant.
(I) Gene Ontology enrichment analysis of genes upregulated in $CD34^+Sca\text{-}1^+$ ECs, highlighting functional categories such as stem cell development, differentiation, and somatic stem cell maintenance.
(J) The schematic illustration depicts the spatial localization of Sca-1, a marker for mesenchymal or hematopoietic stem cells, and $CD34^+Sca\text{-}1^+CD31^+$ endothelial cells as the trunk of the Periportal Lamellar Complex (PLC).

## $CD34^+Sca\text{-}1^+$ Endothelium in the Periportal Lamellar Complex is potential Regulator of Spatial Patterning of Intrahepatic Bile Duct Branching during cirrhosis

Our 3D imaging showed that terminal bile duct branches are spatially colocalized with PLC structures around the main portal vein axis(Figures S5A-C). Volcano plot analysis identified multiple genes in the PLC endothelium associated with bile duct development and functional regulation, including JCAD, DLL4, and HES1 (Figure 5A). Gene Ontology enrichment analysis confirmed that differentially expressed genes in the $CD34^+Sca\text{-}1^+$ endothelium of PLC are enriched in pathways regulating epithelial morphogenesis and branching morphogenesis of epithelial tubes, suggesting multifunctional roles of PLC in bile duct branching and hepatic microenvironment homeostasis (Figure 5B)

During liver fibrosis progression, proliferation and infiltration of terminal bile duct branches (Canals of Hering, CoH) into the hepatic parenchyma represent a core feature of the intrahepatic ductular reaction (DR), critically influencing disease progression,

liver regeneration, and carcinogenesis[34-36]. To investigate the potential regulatory role of the PLC structures in bile duct growth, we established a $CCl_4$-induced mouse model of liver fibrosis/cirrhosis. The results showed:(1)Using MCNP-Pink to label the portal vein combined with three-dimensional DAB immunohistochemical staining for CK19 to visualize bile duct epithelial cells, extended depth-of-field brightfield imaging revealed that in control mice, bile duct termini localized adjacent to the portal vein, whereas after 3 or 6 weeks of $CCl_4$ treatment, bile duct termini significantly extended into the hepatic parenchyma by 100–300 μm (Figures 5C and 5D), with a notable increase in bile duct branch area (Figure S5C). (2)Multiplex CmTSA 3D imaging demonstrated that under fibrotic conditions, PLC structures became elongated and extended toward the lobular parenchyma. Concurrently, the $CD34^+Sca\text{-}1^+$ endothelial cell population of PLC, showed a significant increase during liver fibrosis progression (Figure S5D). (3)Further 3D staining confirmed that under fibrotic conditions, bile ducts progressively grew and branching along the expanded PLC structures and infiltrated deeper into the hepatic lobules, forming extensive terminal bile duct branches within the parenchyma. (4)With advancing fibrosis, the extension of $CK19^+$ bile duct termini into the parenchyma was markedly greater after 6 weeks of $CCl_4$ treatment compared to 3 weeks, suggesting a coordinated expansion of bile duct branches alongside PLC structures that correlates with fibrosis severity (Figures 5E and 5F).

Moreover, single-cell transcriptomic analysis revealed significant upregulation of bile duct-related genes in the $CD34^+Sca\text{-}1^+$ endothelium of PLC in cirrhotic liver, with notably high expression of Lgals1 (Galectin-1) and HGF(Figure 5G). Previous studies have shown that Galectin-1 is absent in normal liver parenchyma but highly expressed in intrahepatic cholangiocarcinoma (ICC), correlating with tumor dedifferentiation and invasion[37, 38]. Additionally, hepatocyte growth factor (HGF), particularly in combination with epidermal growth factor (EGF) in 3D cultures, promotes hepatic progenitor cells to form bile duct-polarized cystic structures[39]. Together, these findings suggest the PLC endothelium may act as a key regulator of bile duct branching and fibrotic microenvironment remodeling in liver cirrhosis.

Collectively, our results demonstrate that the PLC, situated between the portal vein and periportal sinusoidal endothelium, constitutes a critical vascular

microenvironmental unit. It not only guides bile duct branching during development but also, through its basal $CD34^+Sca\text{-}1^+$ double-positive endothelial cells, orchestrates bile duct epithelial proliferation, branching morphogenesis, and bile acid transport homeostasis via multiple signaling pathways. Particularly during liver fibrosis progression, the PLC exhibits dynamic structural extension correlating with fibrosis severity, serving as a spatial scaffold facilitating terminal bile duct migration and expansion into the hepatic parenchyma (Figure 5H). These findings highlight the PLC endothelial cell population and the vascular-bile duct interface as key regulatory hubs in bile duct regeneration, tissue repair, and pathological remodeling, providing novel cellular and molecular insights for understanding bile duct-related diseases such as ductular reaction, cholangiocarcinoma, and cholestatic disorders, and offering potential targets for therapeutic intervention.

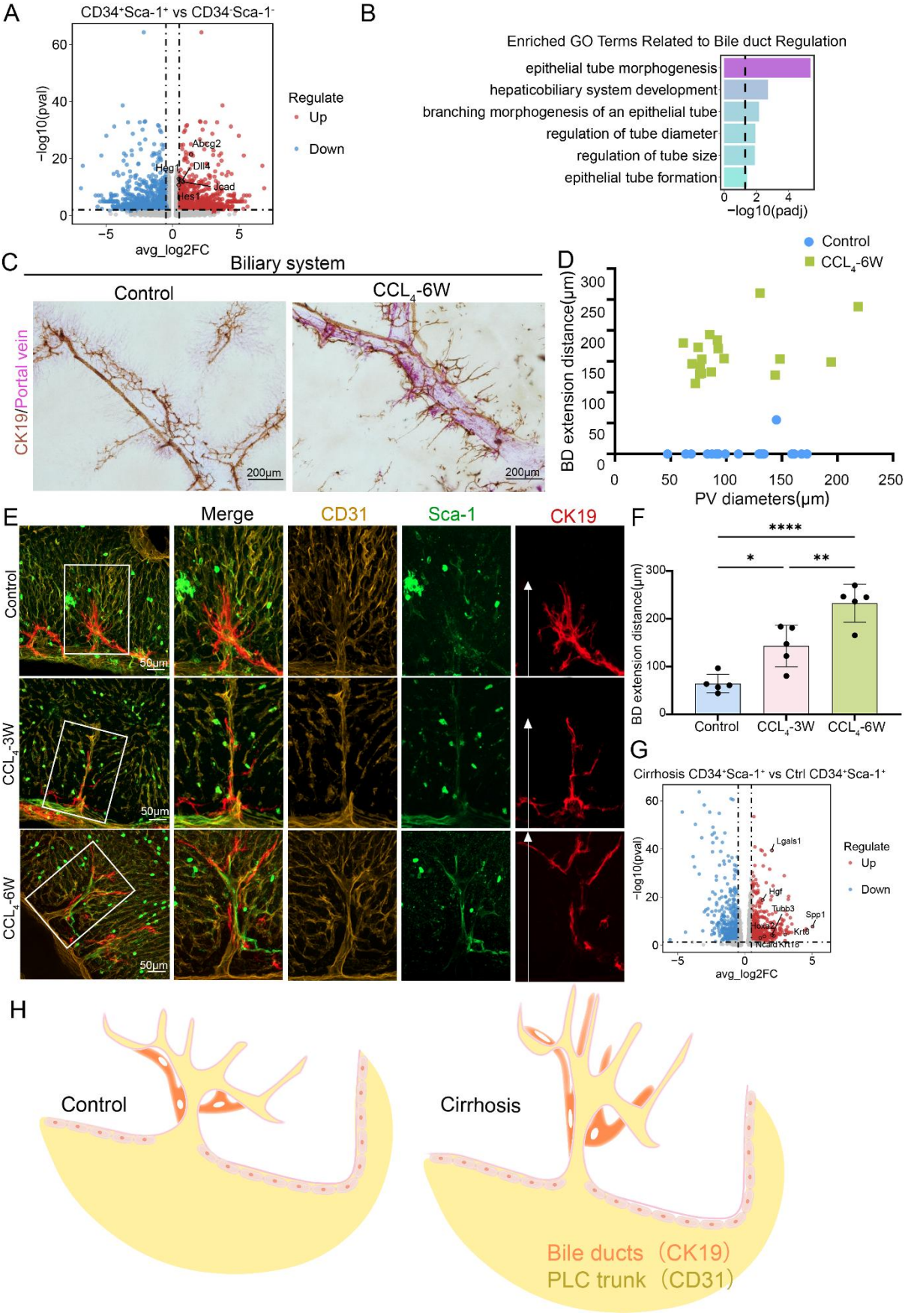


**Figure 5. CD34⁺Sca-1⁺ Endothelium in the Periportal Lamellar Complex is potential Regulator of Spatial Patterning of Intrahepatic Bile Duct Branching during cirrhosis.**

(A) Volcano plot of differentially expressed bile duct-related genes in $CD34^+Sca\text{-}1^+$ double-positive cells. The x-axis represents log2 fold change (log2FC), and the y-axis represents -log10 adjusted *P* value (-log10(P-adjust)). Genes significantly upregulated are located in the upper right quadrant.
(B) Functional enrichment analysis of upregulated genes in $CD34^+Sca\text{-}1^+$ cells, showing enriched categories such as epithelial morphogenesis and branching morphogenesis of epithelial tubes, represented by -log10(*P* value).
(C) Visualization of portal vein labeled with MCNP-Pink and bile duct epithelial cells stained for CK19 (brown) by 3D DAB immunohistochemistry in control and $CCl_4$ 6-week fibrotic mice. Scale bar: 200 μm.
(D) Quantification of the distance that bile duct termini extend from portal vein surfaces into hepatic parenchyma in control and $CCl_4$ 6-week mice, presented as mean ± SD (control n=20, $CCl_4$ 6-week n=18).
(E) Multiplex immunofluorescence showing expression and spatial distribution of CD31 (yellow), Sca-1 (green), and CK19 (red) in control and fibrotic models ($CCl_4$ 3-week and 6-week). White arrows in CK19 single-channel magnified images indicate bile duct termini. Scale bar: 50 μm.
(F) Quantitative measurement of bile duct termini extension distances along PLC structures into hepatic parenchyma in control, early ($CCl_4$ 3-week), and late ($CCl_4$ 6-week) fibrosis mice. Data represent mean ± SD (n=5 per group). Statistical significance determined by one-way ANOVA with Tukey's multiple comparisons test; *P < 0.05, **P < 0.01, ****P < 0.0001.
(G) Volcano plot of differentially expressed bile duct-related genes in $CD34^+Sca\text{-}1^+$ cells from fibrotic livers compared to controls. Axes as in (A). Significantly upregulated genes are in the upper right quadrant.
(H) Schematic illustration showing spatial localization of CK19 and CD31 within the PLC structure.

## $CD34^+Sca\text{-}1^+$ Endothelium in the Periportal Lamellar Complex is a Potential Neurovascular Niche Regulating Hepatic Autonomic Nerve Patterning in Cirrhosis

The liver receives both afferent and efferent innervation from sympathetic and parasympathetic nerve fibers. Although hepatic nerve distribution exhibits species-specific differences, In the human liver, nerve fibers are predominantly localized around the portal vein and central vein regions, and terminal nerve cells can also be observed within the interlobular septa and the connective tissue of the parenchyma. In contrast, in mice and rats, hepatic innervation is almost exclusively confined to the portal vein area (Figure S6A)[6, 40]. How the autonomic nervous system regulates liver function in mice despite the apparent absence of substantive nerve fiber invasion into the parenchyma remains unclear.

In this study, we identified that the $CD34^+Sca\text{-}1^+$ endothelium of PLC exhibits prominent neurodevelopmental molecular features. Differential gene expression analysis revealed significant upregulation of multiple genes associated with neurogenesis and axon guidance within this population (Figure 6A), including *Nrg1*—a

key regulator of Schwann cell proliferation, myelination, and sheath formation—and *ADGRG6* (Gpr126), an essential factor for myelination in the mammalian peripheral nervous system, required for Schwann cell differentiation and peripheral nerve development in mice[41]. Subsequent GO enrichment analysis of differentially expressed genes (DEGs) in this cell cluster demonstrated significant activation of pathways related to neuronal projection and central nervous system differentiation (Figure 6B).

Previous studies have confirmed that the highest density of hepatic parenchymal innervation originates from postganglionic sympathetic neurons located in the celiac ganglion[42]. Tyrosine hydroxylase (TH) immunohistochemistry is the preferred method to visualize noradrenergic sympathetic innervation of hepatocytes and vasculature in both rodents and humans[43]. In this study, confocal three-dimensional imaging revealed that $TH^+$ sympathetic nerve fibers form a characteristic "neuronal bead-chain" network along the PLC structure, with nerve terminals terminating at the PLC base and around vascular bundles, suggesting a potential regulatory role of the PLC in controlling functional zones within the hepatic lobule (Figures 6C, S6B and S6C).

Further validation using a $CCl_4$-induced mouse liver fibrosis model demonstrated that: (1) during fibrosis progression, sympathetic nerve fibers progressively extend along the PLC structure, accompanied by nerve terminal branching and infiltration into the hepatic parenchyma; (2) after 6 weeks of $CCl_4$ treatment, $TH^+$ nerve fibers extended significantly farther into the hepatic parenchyma compared to 3 weeks, indicating a coordinated expansion trend of bile duct branches, PLC structures, and sympathetic nerve networks closely associated with fibrosis severity (Figures 6D and 6E).

Furthermore, single-cell transcriptomic volcano plot analysis revealed significant upregulation of neural-related genes within the $CD34^+Sca\text{-}1^+$ endothelium of PLC in the cirrhotic group, notably including *EDNRB* (Endothelin receptor type B), which plays a critical role in the development of neural crest-derived autonomic nervous system components, including the liver[39]. Nestin, a type VI intermediate filament protein predominantly expressed in the central nervous system, has recently been implicated in tissue homeostasis during wound healing. For example, in traumatic CNS injury, Nestin is induced in reactive astrocytes contributing to glial scar formation. Additionally,

Nestin expression correlates with the severity of renal tubulointerstitial fibrosis. In the healthy adult liver, Nestin is nearly absent but is upregulated following acute or chronic hepatic injury, indicating its potential role in liver regeneration(Figure 6F)[44]. These findings suggest that this specific endothelial subpopulation of PLC may participate in neural branching development and fibrotic microenvironment remodeling, exhibiting multifunctional regulatory potential(Figure 6G).

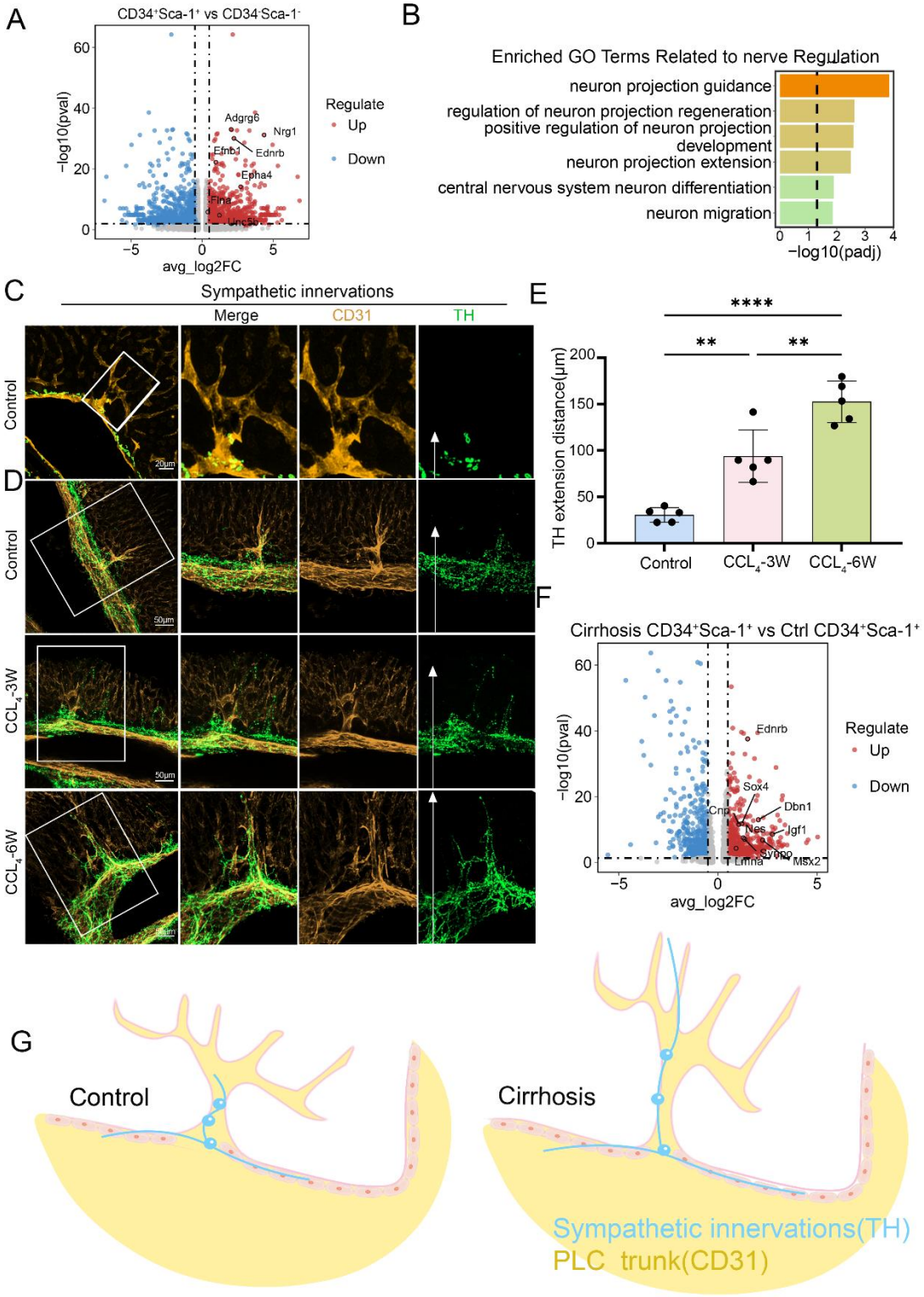


**Figure 6. CD34⁺Sca-1⁺ Endothelium in the Periportal Lamellar Complex is a Potential Neurovascular Niche Regulating Hepatic Autonomic Nerve Patterning in Cirrhosis**

(A) Differential expression analysis of nerve-related genes in CD34⁺Sca-1⁺ endothelial cells. The x-axis indicates log2 fold change (log2FC), and the y-axis represents –log10 adjusted P value (–log10(P-adjust)). Significantly upregulated genes are located in the upper right quadrant.

(B) Gene ontology (GO) enrichment analysis of upregulated genes in CD34⁺Sca-1⁺ cells, showing enrichment in

functional categories such as semaphorin-plexin mediated axon guidance, regulation of neuronal projection regeneration, and modulation of postsynaptic neurotransmitter receptor endocytosis. Enrichment significance is indicated by –log10(P-value).

(C) Multiplex immunofluorescence staining showing tyrosine hydroxylase (TH, green) labeling sympathetic nerves and CD31 (yellow) labeling portal vein endothelium. Scale bar: 20 μm.

(D) Distribution of CD31 (yellow) and TH (green) expression in control and $CCl_4$-induced liver fibrosis models at week 3 and week 6, visualized by multiplex immunofluorescence. In the green channel images, the white arrows marks the terminal location of TH-positive sympathetic nerve endings. Scale bar: 50 μm.

(E) Quantification of the distance from sympathetic nerve endings to the hepatic parenchyma along PLC structures in control, early fibrosis ($CCl_4$-3 weeks), and advanced fibrosis ($CCl_4$-6 weeks) mice. Data are presented as mean ± standard deviation (Mean ± SD), n=5 per group. Statistical analysis was performed using one-way ANOVA followed by Tukey's multiple comparison test; *$P < 0.05$, **$P < 0.01$, ****$P < 0.0001$.

(F) Differential expression analysis of nerve-related genes between $CD34^+Sca\text{-}1^+$ cells from cirrhotic and control livers. The x-axis indicates log2 fold change (log2FC), and the y-axis represents –log10 adjusted P value (–log10(P-adjust)). Significantly upregulated genes are located in the upper right quadrant.

(G) Schematic diagram illustrating the spatial localization of TH-positive sympathetic nerves and CD31-positive endothelial cells within PLC structures.

## DISCUSSION

Accurate three-dimensional mapping of organs in both physiological and pathological states is essential for understanding their function and disease mechanisms. Compared to flow cytometry and conventional two-dimensional histology, building a comprehensive multi-channel 3D atlas of the liver helps compensate for spatial information loss—especially important for its complex and heterogeneous ductal-vascular systems. This study addresses two major technical bottlenecks in 3D imaging of the mouse liver. First, although various tissue-clearing techniques (e.g., SeeDB, iDISCO, CUBIC, Clarity, and PEGASOS) have been applied to whole-organ imaging[16, 45, 46], he liver's high content of heme, lipids, and dense connective tissue renders it significantly less transparent than organs like the brain. Second, current imaging platforms often face trade-offs between resolution and field of view. For example, CT and PCCT are limited to single-system visualization, while DUCT enables dual-system reconstruction but cannot resolve fine structures such as bile canaliculi due to its 5 μm/pixel resolution[9, 11].

To overcome these challenges, we developed the Liver-CUBIC 3D visualization system. By optimizing $H_2O_2$-based bleaching and urea concentration, we significantly improved hepatic tissue transparency (total clearing time: 3.25 days; light transmittance increased by 20.12%). In parallel, we introduced multicolor metal compound nanoparticles (MCNPs) with excellent photostability and $H_2O_2$ resistance to achieve four-channel segmentation and labeling of the portal vein, hepatic artery, central vein, and bile ducts. This system enables, for the first time, 3D visualization of microstructures such as terminal bile duct arborization, fine portal vein branching patterns, and fenestrations in central venous endothelium—providing a high-resolution, multidimensional platform for liver microcirculation studies.

The labeling strategy relies on perfusing contrast-complementary MCNPs into multiple vascular and ductal compartments. By carefully controlling injection site, pressure, and volume—combined with 15 μL microinjection needles and post-perfusion vessel ligation—we ensured even dye distribution and structural fidelity. High-density image data can be simplified using dual-channel overlays (e.g., portal vein and bile duct), and multiple imaging modalities (e.g., stereomicroscopy, confocal, or

extended-depth microscopy) can be chosen depending on the desired resolution or field of view. Moreover, the dyes demonstrate robust fluorescence under laser-scanning microscopy, enabling clear 3D structural imaging.

Despite its strengths, the system remains sensitive to anatomical variation, such as liver lobe overlap and heterogeneous vascular architecture. Local perfusion may be inconsistent or excessively aggregated, especially at vascular intersections. Therefore, injection strategies and perfusion parameters must be adapted to liver size and vessel status to improve reproducibility and image quality.

Using this system, we identified a previously unrecognized structure located on the adventitia of the main portal vein, which we termed the **Periportal Lamellar Complex (PLC)**. The PLC consists of multi-branched extensions radiating from the outer membrane of the main portal vein. Notably, it is absent in terminal vessels and other vascular systems, challenging the conventional "strict hierarchical bifurcation" model of vascular organization. The PLC is spatially associated with terminal branches of both bile ducts and hepatic arteries, suggesting possible roles in local microenvironmental regulation through physical or signaling interactions.

Multiplex immunostaining revealed that cholangiocytes extend along ZO-1$^+$ bile canalicular networks but display an elongated, immature morphology without forming complete lumens (Fig. 3F). This observation aligns with previous findings that HNF4α$^+$ hepatocytes and CK19$^+$ cholangiocytes can jointly form bile-excreting conduits, supporting a guiding role for the PLC in bile duct positioning and morphogenesis[47].

Morphologically, the PLC shares features with previously described **telocytes (TCs)**—a recently identified class of interstitial cells in the liver observed via transmission electron microscopy and immunohistochemistry as CD34$^+$ cells with multiple long telopodes[48, 49]. However, functional and molecular characterization of TCs remains limited, and their direct relationship with the PLC is yet to be determined.

Single-cell transcriptomic analysis revealed a CD34$^+$Sca-1$^+$ endothelial cell population enriched within the PLC that expressed hematopoiesis-related genes and stem cell regulatory pathways[22]. This suggests that the PLC may not only provide structural support but also serve as a perivascular stem cell niche specific to the portal

region, potentially involved in hematopoiesis and tissue regeneration. Supporting this, Sca-1 expression is localized to the portal region during mouse liver development [50], and Nestin$^+$NG2$^+$ precursor cells in the fetal liver also concentrate near the portal vein, where they express key HSC-supportive factors such as SCF and CXCL12[44] — highlighting the PLC as a key component of the hepatic vascular-stem cell microenvironment.

Further analysis showed significant upregulation of genes involved in neurodevelopment and axonal guidance in the CD34$^+$Sca-1$^+$ cluster, along with activation of neuronal signaling pathways. Immunostaining confirmed the presence of TH$^+$ sympathetic nerve fibers wrapping around the PLC in a “beads-on-a-string” pattern (Fig. 6), consistent with a classic neurovascular unit[43]. Previous studies have shown that sympathetic nerves enter the liver along collagen fibers of Glisson’s capsule and interact with hepatic arteries, portal veins, and bile duct epithelium, supporting the PLC as a scaffold for intrahepatic neurovascular integration.

In $CCl_4$-induced hepatotoxic fibrosis models, injury and toxic metabolite accumulation are primarily restricted to the centrilobular region, while bile ducts extend linearly toward the central vein[51, 52]. We observed dynamic elongation of the PLC in parallel with fibrosis progression, indicating its role as a spatial scaffold for ductal expansion. This suggests potential involvement in ductular reactions and neural remodeling during cirrhosis.

In conclusion, this study provides the first systematic characterization of the PLC as a structural and functional interface among hepatic vasculature, bile ducts, and nerves. The PLC serves as a directional scaffold for ductal growth, a specialized stem cell niche, and a potential site of neurovascular coupling. These findings provide novel insights into hepatic homeostasis, bile duct development, and fibrotic remodeling, and suggest that the PLC and its CD34$^+$Sca-1$^+$ endothelial population may represent promising therapeutic targets for diseases such as cholangiocarcinoma and primary sclerosing cholangitis.

STAR★METHODS

KEY RESOURCES TABLE

| REAGENT or RESOURCE | SOURCE | IDENTIFIER |
|---|---|---|
| **Antibodies** | | |
| rabbit Monoclonal anti-CK19 | HUABIO | Cat# ET1601-6,RRID: AB_3069617 |
| rabbit Monoclonal anti-CD31 | Abcam | Cat# ab182981 |
| rabbit Monoclonal anti-HNF4A | HUABIO | Cat#HA721006,RRID: AB_3072131 |
| rabbit Polyclonal anti-ZO-1 | HUABIO | Cat# 21773-1-AP,RRID：AB_10733242 |
| rabbit Monoclonal anti-CD34 | HUABIO | Cat# ET1606-11,RRID: AB_2924309 |
| rabbit Monoclonal anti-LY6A（Sca-1） | HUABIO | Cat# ET1703-67,RRID: AB_3070422 |
| rabbit Monoclonal anti-TH | AiFang biological | Cat# AFRM0092 |
| rabbit Monoclonal anti-CD36 | HUABIO | Cat# ET1701-24,RRID:AB_3070192 |
| rabbit Monoclonal anti-PDGFR beta | HUABIO | Cat# ET1605-20,RRID: AB_3069707 |
| rabbit Monoclonal anti-a-SMA | HUABIO | Cat#ET1607-53, RRID:AB_3069772 |

## EXPERIMENTAL MODEL AND STUDY PARTICIPANT DETAILS

### Animals

All animal procedures were approved by the Institutional Animal Care and Use Committee of Sichuan University. Eight-week-old male wild-type mice (purchased from Beijing Huafukang Bioscience Co., Ltd.) were used to establish a progressive liver fibrosis model. Mice were intraperitoneally injected with carbon tetrachloride ($CCl_4$, 1 mL/kg body weight, $CCl_4$:olive oil = 1:4, v/v, Damas-beta, CAS:56-23-5) twice a week for 3 or 6 weeks (n=3 per group). Control mice received an equal volume of olive oil injection for 3 or 6 weeks (n=3 per group).

### Four-Channel Vascular Typing Labeling and Bile Duct High-Pressure Dye Perfusion in Mice

Step 1: Mice were euthanized by intraperitoneal (IP) injection of sodium pentobarbital at a dose of 100–150 mg/kg body weight.
Step 2: The chest muscles were incised to expose the heart. A perfusion needle was inserted into the left ventricle, ensuring entry into the cardiac cavity.
Step 3: Sequential perfusion was performed with 40 mL of pre-chilled PBS (5 mL/min) to clear blood, followed by 20 mL of 4% paraformaldehyde (5 mL/min) for in situ fixation.
Step 4: The abdominal skin and muscles were cut to the mid-axillary line to expose the liver. The intestines were gently displaced with sterile swabs to fully expose the common bile duct.
Step 5: According to experimental design, the hepatic artery, bile duct, portal vein, and inferior vena cava were selectively labeled with metallic nanoparticle (MCNP) dyes of different colors.

- Hepatic artery: MCNP-Yellow was injected slowly via the left ventricle using a micro-syringe (25 μL, outer needle diameter 0.31 mm, Shanghai Bolige Industrial Co., Ltd.) until complete arterial filling or resistance occurred.

- Bile duct: After blunt separation of the common bile duct and portal vein, MCNP-Green was retrogradely injected via the extrahepatic bile duct until surface bile ducts were fully filled or resistance was felt. The bile duct was ligated with 5-0 suture.
- Portal vein: MCNP-Pink was injected via the portal vein using a micro-syringe until filling or resistance, followed by ligation.
- Inferior vena cava: MCNP-Black was retrogradely injected via the inferior vena cava, followed by ligation.

  Step 6: The liver was harvested and fixed at 4°C for 48 hours before proceeding with tissue clearing procedures.

  Step 7: Labeled liver tissues were sectioned to desired thickness and imaged using a high-magnification deep-focus microscope (Keyence), confocal laser scanning microscope (Zeiss LSM980), or THUNDER high-resolution imaging system (Leica).

Bile Duct High-Pressure Dye Perfusion:
Follow steps 1–4 as above. Then, using a micro-syringe, retrograde catheterization was performed via the extrahepatic bile duct with secure positioning at the hepatic hilar bile duct. A large volume of MCNP-Green was rapidly injected until the entire bile duct system and peripheral branches were filled, evident from surface dye visualization. Dye volume was adjusted to liver size, typically 25–40 μL per mouse.

**Traditional CUBIC Reagent Preparation and Tissue Clearing**

Based on Hiroki R. Ueda's protocol [15]:
Step 1: Prepare ScaleCUBIC-1 (25% CUBIC-I): 25 wt% urea, 25 wt% N,N,N',N'-tetrakis(2-hydroxypropyl)ethylenediamine, and 15 wt% Triton X-100. Prepare ScaleCUBIC-2 (25% CUBIC-II): 50 wt% sucrose, 25 wt% urea, 10 wt% triethanolamine, and 0.1% (v/v) Triton X-100.
Step 2: Fixed liver lobes were immersed in 20 g of CUBIC-I at 37°C with gentle shaking for 3 days, then replaced with fresh CUBIC-I for another 2 days. Samples were rinsed with PBS and immersed in CUBIC-II for 3 days.

**Liver-CUBIC (40%CUBIC+$H_2O_2$) Reagent Preparation and Tissue Clearing**

Step 1: Prepare 40%CUBIC-I: 36 wt% urea, 25 wt% N,N,N',N'-tetrakis(2-hydroxypropyl)ethylenediamine, and 15 wt% Triton X-100. Prepare 40%CUBIC-II: 50 wt% sucrose, 35 wt% urea, 10 wt% triethanolamine, and 0.1% Triton X-100. Bleaching solution: 4.5% hydrogen

peroxide and 24 mM sodium hydroxide.
Step 2: Whole liver lobes were immersed in IRISKit® HyperView Quench Buffer (#MH010301) at room temperature for 24 h with solution refreshed every 12 h. Samples were then washed with PBS and incubated in 20 g of 40%CUBIC-I at 37°C for 1 day, washed again, and finally incubated in 40%CUBIC-II at 37°C for 1 day.

**Transmission Quantification**

Transmittance was measured using a microplate reader (BioTek, USA) on 1 mm-thick liver sections.
Step 1: 1 mm liver slices were cut into 5 mm × 5 mm squares and treated with various clearing protocols, then immersed in CUBIC-II. Five replicates per group were placed into 96-well plates.
Step 2: Optical transmittance was recorded from 400 nm to 900 nm, generating transmittance spectra for each sample.

**3D DAB Staining and Imaging**

Step 1: Liver tissues were fixed in 4% paraformaldehyde at 4°C for 24 h, sectioned to 200 μm using a vibratome (Leica VT1200, Germany), and washed three times in distilled water (10 min each).
Step 2: Sections were delipidated in acetone:chloroform (1:1, v/v) for 3 h.
Step 3: Dehydrated in graded ethanol (75%, 85%, 95%, 100%, 100%, 95%, 85%, 75%), 30 min each, followed by three 10 min water washes.
Step 4: Quenching was performed with quench reagent (including $H_2O_2$, IRISKit HyperView Quench Buffer) for 20 min in a LUMINIRIS quencher, followed by three water washes. Sections were treated with 2% EDTA antigen retrieval buffer (in distilled water) at 37°C for 35 min, then washed with PBS + 0.3% Triton X-100 three times (10 min each).
Step 5: Incubated with primary antibody (rabbit anti-CK19, 1:2000, Huaan Biotechnology ET1601-6) at 4°C for 24 h, followed by three PBS washes.
Step 6: Incubated with polymerized HRP-conjugated secondary antibody at 4°C for 24 h, followed by PBS + 0.3% Triton washes.
Step 7: Stained with DAB (Zhongshan Jinqiao ZLI-9017) for 10 min, followed by three PBS washes.
Step 8: Sequentially cleared with 40%CUBIC-I at 37°C for 30 min, washed, and incubated in 40%CUBIC-II at 37°C for 30 min.
Step 9: 3D imaging was performed using a high-depth focus microscope.

**3D TSA Multiplex Immunofluorescence Staining**

Performed using IRISKit® HyperView multiplex immunostaining kit (#MH010101).

Steps 1–4: Same as 3D DAB protocol.

Step 5: Incubated with primary antibodies (anti-CK19, CD31, HNF4α, ZO-1, CD34, Sca-1, and TH) overnight at 4°C.

Step 6: Incubated with polymerized HRP-conjugated secondary antibody overnight at 4°C.

Step 7: Sequentially visualized each antibody with specific TSA fluorophores: Cyclic-480 (EX 465–495 nm, EM 512–558 nm), Cyclic-550 (EX 540–560 nm, EM 575–595 nm), and Cyclic-630 (EX 620–640 nm, EM >665 nm).

Step 8: After each round, antibodies were stripped using IRISKit® HyperView advanced antibody removal kit.

Step 9: Cleared tissue was imaged by confocal laser scanning microscopy (Zeiss LSM980).

**Single-Cell Data Mining**

We re-analyzed published single-cell transcriptomic datasets of liver endothelial cells (ECs) sorted by FACS from three normal mouse livers [22].

**Statistics and Reproducibility**

Statistical analyses were performed using Prism 8.0 (GraphPad Software, Inc.). p-values are indicated in figure legends. Data are presented as mean ± SD unless otherwise stated. Two-group comparisons were made using Student's t-test. One-way ANOVA followed by Tukey's multiple comparisons test was used for multi-group analysis. Statistical significance was defined as ***$p < 0.001$, **$p < 0.01$, *$p < 0.05$.

**Data Availability**

The original data can be obtained by contacting the corresponding author, Chengjian Zhao (chjianzhao@scu.edu.cn). Additional relevant data can be found in the Materials and Methods section.

**Acknowledgements**

This study was supported by multiple funding sources, including the National Natural Science Foundation of China (grant no. 82270542) and the Natural Science Foundation of Sichuan Province (grant no. 2023NSFSC0665).

**Author Contributions**

Tongtong Xu and Fujun Cao contributed equally to this work. Tongtong Xu was responsible for the

conception and design of the study. Fujun Cao and Tongtong Xu performed the experiments. Ruihan Zhou was responsible for bioinformatics data analysis. Qin Chen and Jian Zhong participated in image acquisition. Yulin Wang, Chaoxin Xiao, and Banglei Yin contributed to manuscript writing. Chengjian Zhao oversaw the entire project and approved the final version of the manuscript.

**Competing Interests:** The authors declare no conflicts of interest

**REFERENCES**


[1] OZOUGWU J. Physiology of the liver [J]. 2017, 4(13-24.

[2] ALMAZROO O A, MIAH M K, VENKATARAMANAN R. Drug Metabolism in the Liver [J]. Clinics in liver disease, 2017, 21(1): 1-20.

[3] KALRA A Y E, WEHRLE CJ, ET AL. Physiology, Liver [M]. StatPearls [Internet]. Treasure Island (FL); StatPearls Publishing. 2023.

[4] YAP K K, MITCHELL G M. Chapter One - Recapitulating the liver niche in vitro [M]//NILSSON S. Advances in Stem Cells and their Niches. Elsevier. 2022: 1-55.

[5] FRIEDMAN S L. Mechanisms of hepatic fibrogenesis [J]. Gastroenterology, 2008, 134(6): 1655-69.

[6] MILLER B M, ODERBERG I M, GOESSLING W. Hepatic Nervous System in Development, Regeneration, and Disease [J]. Hepatology (Baltimore, Md), 2021, 74(6):

[7] ZHANG Q, LI A, CHEN S, et al. Multiscale reconstruction of various vessels in the intact murine liver lobe [J]. Communications biology, 2022, 5(1): 260.

[8] LV W J, ZHAO X Y, HU D D, et al. Insight into Bile Duct Reaction to Obstruction from a Three-dimensional Perspective Using ex Vivo Phase-Contrast CT [J]. Radiology, 2021, 299(3): 597-610.

[9] PEETERS G, DEBBAUT C, FRIEBEL A, et al. Quantitative analysis of hepatic macro- and microvascular alterations during cirrhogenesis in the rat [J]. Journal of anatomy, 2018, 232(3): 485-96.

[10] KIM K H, CHEN C C, ALPINI G, et al. CCN1 induces hepatic ductular reaction through integrin $\alpha v\beta_5$-mediated activation of NF-κB [J]. The Journal of clinical investigation, 2015, 125(5): 1886-900.

[11] HANKEOVA S, SALPLACHTA J, ZIKMUND T, et al. DUCT reveals architectural mechanisms contributing to bile duct recovery in a mouse model for Alagille syndrome [J]. eLife, 2021, 10(

[12] QIN L, ZHAO X, JIAN J, et al. High-resolution 3D visualization of ductular proliferation of bile duct ligation-induced liver fibrosis in rats using x-ray phase contrast computed tomography [J]. Scientific reports, 2017, 7(1): 4215.

[13] SEGOVIA-MIRANDA F, MORALES-NAVARRETE H, KüCKEN M, et al. Three-dimensional spatially resolved geometrical and functional models of human liver tissue reveal new aspects of NAFLD progression [J]. Nature medicine, 2019, 25(12): 1885-93.

[14] MOLINA L M, KRUTSENKO Y, JENKINS N E C, et al. LiverClear: A versatile protocol for mouse liver tissue clearing [J]. STAR protocols, 2022, 3(1): 101178.

[15] SUSAKI E A, TAINAKA K, PERRIN D, et al. Whole-brain imaging with single-cell resolution using chemical cocktails and computational analysis [J]. Cell, 2014, 157(3): 726-39.

[16] TAINAKA K, KUBOTA S I, SUYAMA T Q, et al. Whole-body imaging with single-cell resolution by tissue decolorization [J]. Cell, 2014, 159(4): 911-24.
[17] LIU Z, XU M, HUANG S, et al. Mesoscale visualization of three-dimensional microvascular architecture and immunocyte distribution in intact mouse liver lobes [J]. Theranostics, 2022, 12(12): 5418-33.
[18] MAK K M, SHIN D W. Hepatic sinusoids versus central veins: Structures, markers, angiocrines, and roles in liver regeneration and homeostasis [J]. Anatomical record (Hoboken, NJ : 2007), 2021, 304(8): 1661-91.
[19] ZHANG Y, DEBOSCH B J. A protocol to induce systemic autophagy and increase energy metabolism in mice using PEGylated arginine deiminase [J]. STAR protocols, 2022, 3(3): 101489.
[20] DE JONG I E M, VAN DEN HEUVEL M C, WELLS R G, et al. The heterogeneity of the biliary tree [J]. Journal of hepatology, 2021, 75(5): 1236-8.
[21] BANALES J M, HUEBERT R C, KARLSEN T, et al. Cholangiocyte pathobiology [J]. Nature reviews Gastroenterology & hepatology, 2019, 16(5): 269-81.
[22] SU T, YANG Y, LAI S, et al. Single-Cell Transcriptomics Reveals Zone-Specific Alterations of Liver Sinusoidal Endothelial Cells in Cirrhosis [J]. Cellular and molecular gastroenterology and hepatology, 2021, 11(4): 1139-61.
[23] HALPERN K B, SHENHAV R, MASSALHA H, et al. Paired-cell sequencing enables spatial gene expression mapping of liver endothelial cells [J]. Nature biotechnology, 2018, 36(10): 962-70.
[24] INVERSO D, SHI J, LEE K H, et al. A spatial vascular transcriptomic, proteomic, and phosphoproteomic atlas unveils an angiocrine Tie–Wnt signaling axis in the liver [J]. Developmental cell, 2021, 56(11): 1677-93.e10.
[25] PETERSEN B E, GROSSBARD B, HATCH H, et al. Mouse A6-positive hepatic oval cells also express several hematopoietic stem cell markers [J]. Hepatology (Baltimore, Md), 2003, 37(3): 632-40.
[26] MORCOS M N F, SCHOEDEL K B, HOPPE A, et al. SCA-1 Expression Level Identifies Quiescent Hematopoietic Stem and Progenitor Cells [J]. Stem cell reports, 2017, 8(6): 1472-8.
[27] TANIGUCHI H, TOYOSHIMA T, FUKAO K, et al. Presence of hematopoietic stem cells in the adult liver [J]. Nature medicine, 1996, 2(2): 198-203.
[28] SUSKIND D L, MUENCH M O. Searching for common stem cells of the hepatic and hematopoietic systems in the human fetal liver: CD34+ cytokeratin 7/8+ cells express markers for stellate cells [J]. Journal of hepatology, 2004, 40(2): 261-8.
[29] AGRAWAL H, MEHATRE S H, KHURANA S. The hematopoietic stem cell expansion niche in fetal liver: Current state of the art and the way forward [J]. Experimental hematology, 2024, 136(104585.
[30] CHRISTODOULOU C, SPENCER J A, YEH S A, et al. Live-animal imaging of native haematopoietic stem and progenitor cells [J]. Nature, 2020, 578(7794): 278-83.
[31] ZHANG Y, STEHLING-SUN S, LEZON-GEYDA K, et al. PR-domain-containing Mds1-Evi1 is critical for long-term hematopoietic stem cell function [J]. Blood, 2011, 118(14): 3853-61.
[32] KIKUCHI A, MONGA S P. PDGFRα in liver pathophysiology: emerging roles in development, regeneration, fibrosis, and cancer [J]. Gene expression, 2015, 16(3): 109-27.

[33] OWEN A, PATTEN D, VIGNESWARA V, et al. PDGFRα/Sca-1 Sorted Mesenchymal Stromal Cells Reduce Liver Injury in Murine Models of Hepatic Ischemia-Reperfusion Injury [J]. Stem cells (Dayton, Ohio), 2022, 40(11): 1056-70.
[34] CLOUSTON A D, POWELL E E, WALSH M J, et al. Fibrosis correlates with a ductular reaction in hepatitis C: roles of impaired replication, progenitor cells and steatosis [J]. Hepatology (Baltimore, Md), 2005, 41(4): 809-18.
[35] STRAZZABOSCO M, FABRIS L. Development of the bile ducts: essentials for the clinical hepatologist [J]. Journal of hepatology, 2012, 56(5): 1159-70.
[36] CARPINO G, CARDINALE V, FOLSERAAS T, et al. Hepatic Stem/Progenitor Cell Activation Differs between Primary Sclerosing and Primary Biliary Cholangitis [J]. The American journal of pathology, 2018, 188(3): 627-39.
[37] SHIMONISHI T, MIYAZAKI K, KONO N, et al. Expression of endogenous galectin-1 and galectin-3 in intrahepatic cholangiocarcinoma [J]. Human pathology, 2001, 32(3): 302-10.
[38] BACIGALUPO M L, MANZI M, RABINOVICH G A, et al. Hierarchical and selective roles of galectins in hepatocarcinogenesis, liver fibrosis and inflammation of hepatocellular carcinoma [J]. World journal of gastroenterology, 2013, 19(47): 8831-49.
[39] TANIMIZU N, MIYAJIMA A, MOSTOV K E. Liver progenitor cells develop cholangiocyte-type epithelial polarity in three-dimensional culture [J]. Molecular biology of the cell, 2007, 18(4): 1472-9.
[40] YI C-X, LA FLEUR S E, FLIERS E, et al. The role of the autonomic nervous liver innervation in the control of energy metabolism [J]. Biochimica et Biophysica Acta (BBA) - Molecular Basis of Disease, 2010, 1802(4): 416-31.
[41] MONK K R, OSHIMA K, JöRS S, et al. Gpr126 is essential for peripheral nerve development and myelination in mammals [J]. Development (Cambridge, England), 2011, 138(13): 2673-80.
[42] MIZUNO K, UENO Y. Autonomic Nervous System and the Liver [J]. Hepatology research : the official journal of the Japan Society of Hepatology, 2017, 47(2): 160-5.
[43] ADORI C, DARAIO T, KUIPER R, et al. Disorganization and degeneration of liver sympathetic innervations in nonalcoholic fatty liver disease revealed by 3D imaging [J]. Science advances, 2021, 7(30):
[44] AHMED J, KUNISAKI Y, MERAD M, et al. Nestin+ Pericytes In The Fetal Liver Are Necessary To Maintain HSCs [J]. Blood, 2013, 122(21): 583.
[45] RENIER N, WU Z, SIMON D J, et al. iDISCO: a simple, rapid method to immunolabel large tissue samples for volume imaging [J]. Cell, 2014, 159(4): 896-910.
[46] QI Y, YU T, XU J, et al. FDISCO: Advanced solvent-based clearing method for imaging whole organs [J]. Science advances, 2019, 5(1): eaau8355.
[47] TANIMIZU N, ICHINOHE N, SASAKI Y, et al. Generation of functional liver organoids on combining hepatocytes and cholangiocytes with hepatobiliary connections ex vivo [J]. Nature communications, 2021, 12(1): 3390.
[48] XIAO J, WANG F, LIU Z, et al. Telocytes in liver: electron microscopic and immunofluorescent evidence [J]. Journal of cellular and molecular medicine, 2013, 17(12): 1537-42.
[49] XU Y, TIAN H, CHENG J, et al. Immunohistochemical biomarkers and distribution of telocytes in ApoE(-/-) mice [J]. Cell biology international, 2019, 43(11): 1286-95.

[50] GOMEZ-SALINERO J M, IZZO F, LIN Y, et al. Specification of fetal liver endothelial progenitors to functional zonated adult sinusoids requires c-Maf induction [J]. Cell stem cell, 2022, 29(4): 593-609 e7.
[51] KANEKO K, KAMIMOTO K, MIYAJIMA A, et al. Adaptive remodeling of the biliary architecture underlies liver homeostasis [J]. Hepatology (Baltimore, Md), 2015, 61(6): 2056-66.
[52] YANG W, HE H, WANG T, et al. Single-Cell Transcriptomic Analysis Reveals a Hepatic Stellate Cell-Activation Roadmap and Myofibroblast Origin During Liver Fibrosis in Mice [J]. Hepatology (Baltimore, Md), 2021, 74(5): 2774-90.

Figure S1

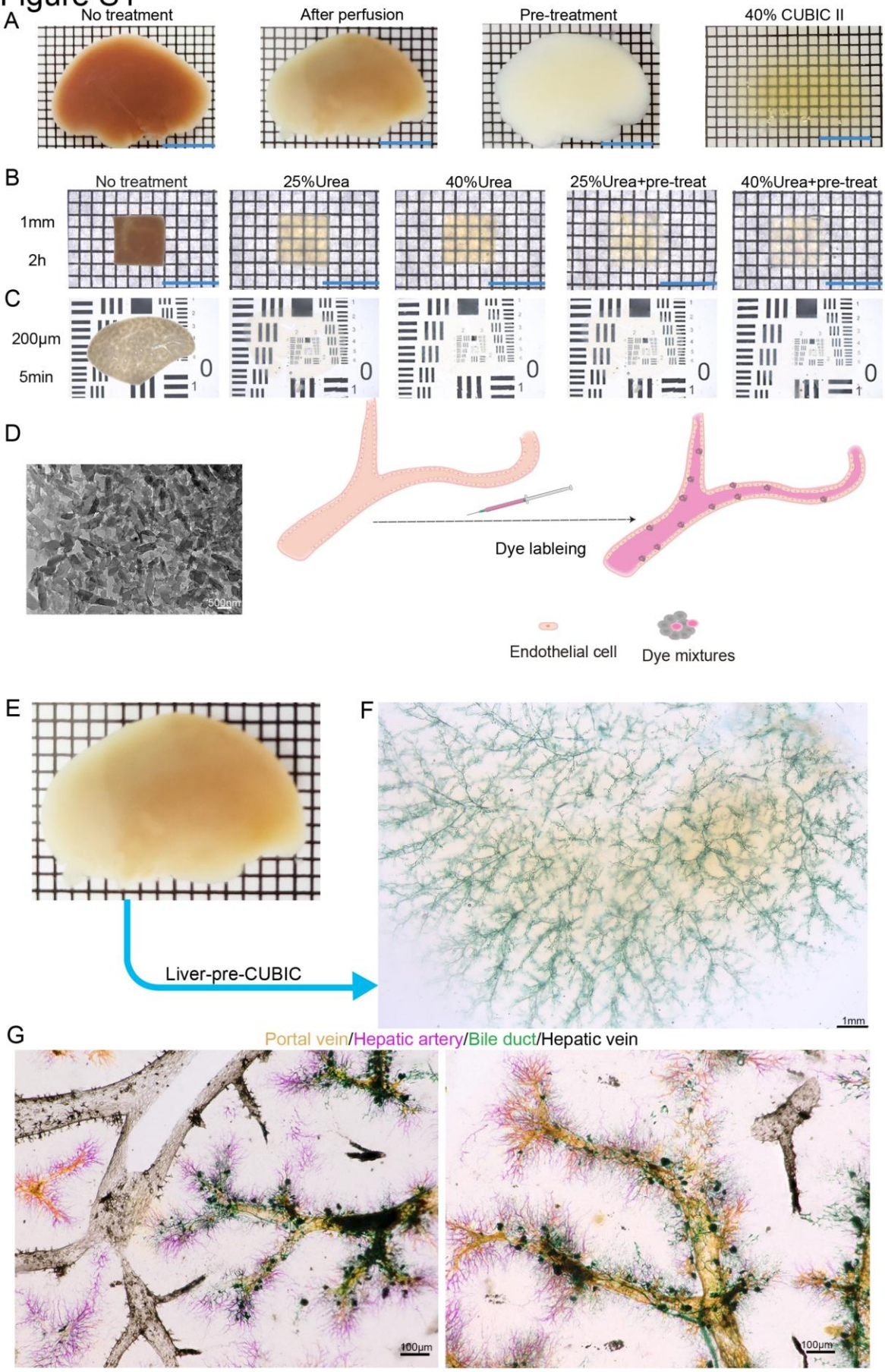
A
No treatment
After perfusion
Pre-treatment
40% CUBIC II
B
No treatment
25%Urea
40%Urea
25%Urea+pre-treat
40%Urea+pre-treat
1mm
2h
C
200μm
5min
D
500nm
Dye lableing
Endothelial cell
Dye mixtures
E
Liver-pre-CUBIC
F
1mm
G
Portal vein/Hepatic artery/Bile duct/Hepatic vein
100μm
100μm

# Supplemental information

**Figure S1.Establishment of a method for simultaneous three-dimensional visualization of the mouse hepatic vascular system, related to Figure 1.**

(A) Key steps of the optimized clearing protocol applied to the left liver lobe: untreated liver lobe (far left), following cardiac perfusion (second from left), after pretreatment (second from right), and after final clearing (far right, using 40% urea + 4.5% $H_2O_2$). Grid size: 1.6 mm × 1.6 mm. Scale bar: 8 mm.

(B) Bright-field images of 1 mm-thick liver samples before and after treatment with four different clearing protocols for 20 minutes. Grid size: 1.6 mm × 1.6 mm. Scale bar: 8 mm.

(C) Bright-field images of 200 μm-thick liver sections before and after treatment with four different clearing protocols for 5 minutes.

(D) Scanning electron microscopy revealed that the metallic compound nanoparticle (MCNP) dyes consisted of aggregates of particles approximately 100 nm in length. After vascular labeling in liver tissue, these dye-pigment complexes adhered densely and uniformly to the vessel walls, forming well-defined labeled structures.

(E–F) Whole-lobe bright-field images of the left liver lobe after bile duct labeling with green dye followed by clearing using the optimized protocol (40% urea + $H_2O_2$). In (E), grid size: 1.6 mm × 1.6 mm. In (F), scale bar: 1 mm.

(G) Three-dimensional reconstructions of the hepatic vascular system: MCNP-Yellow labels the portal vein, MCNP-Pink labels the hepatic artery, MCNP-Green labels the bile duct, and MCNP-Black labels the central vein. Scale bar: 100 μm.

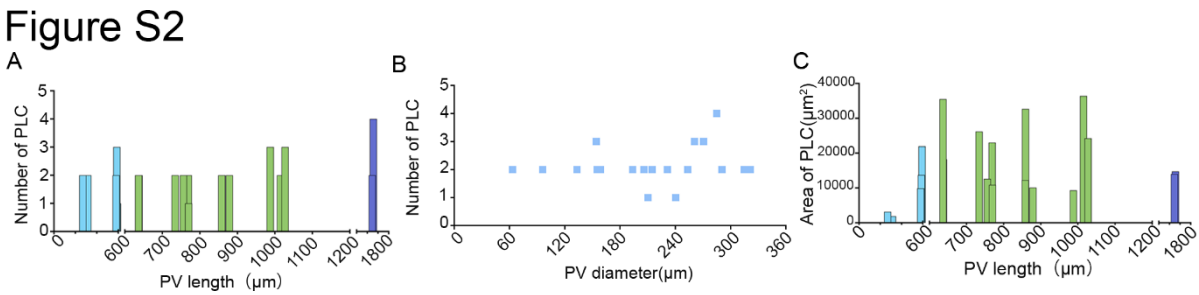


**Figure S2. Analysis of PLC Distribution Along Portal Veins by Length, Diameter, and Area, related to Figure 2.**

(A) Distribution of the number of periportal lamellar complex (PLC) structures along portal vein trunks with lengths ranging from 269.85 μm to 1513.67 μm. Each value represents the number of PLCs embedded along portal veins of a given length.

(B) Distribution of the number of PLC structures along portal vein trunks with diameters ranging from 63.45 μm to 321.42 μm. Each value represents the number of PLCs embedded along portal veins of a given diameter.

(C) Distribution of the total PLC area along portal vein trunks with lengths ranging from 269.85 μm to 1513.67 μm. Each value represents the cumulative area of PLC structures associated with portal veins of a given length.

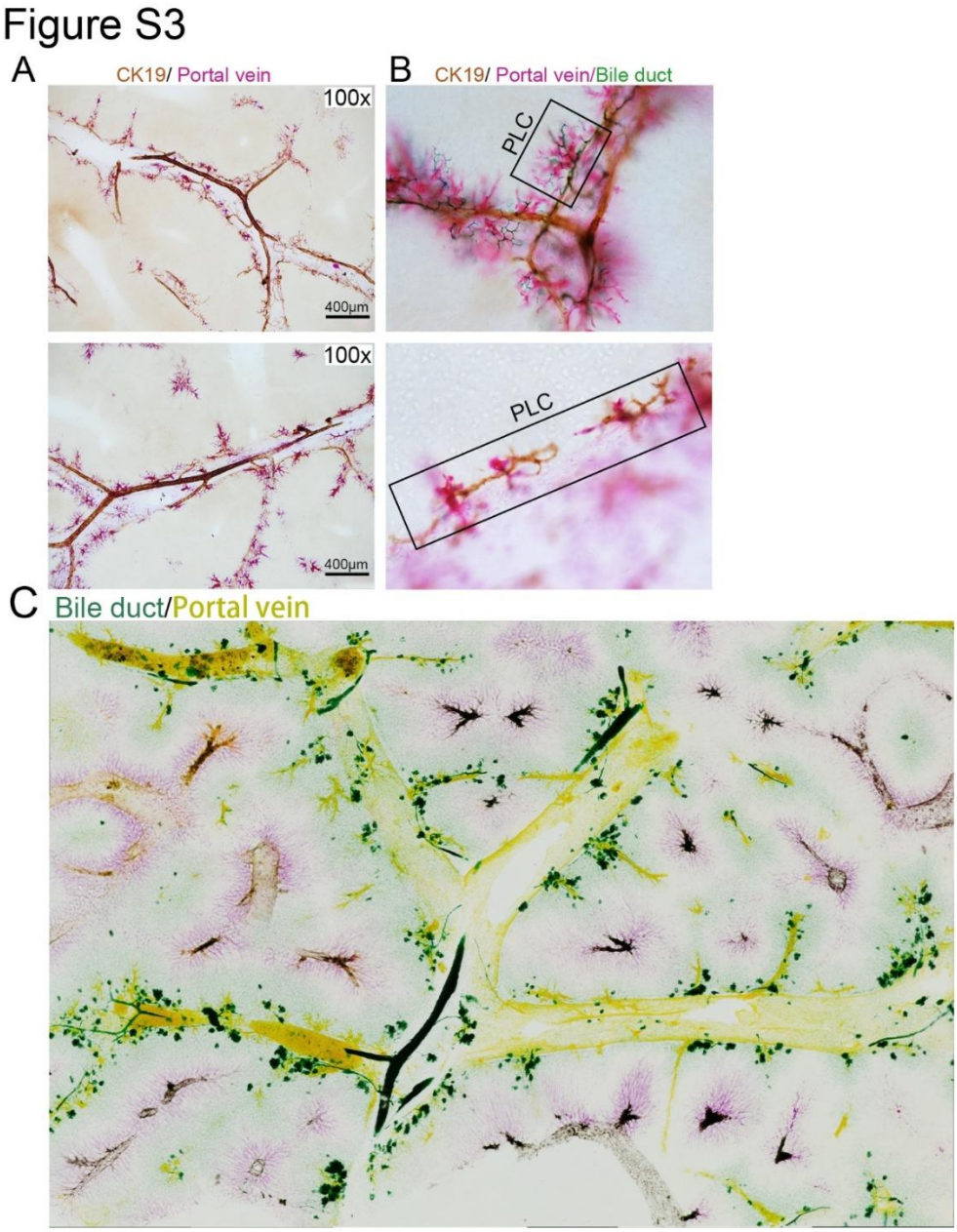


**Figure S3. Interactions Between PLC Structures and Terminal Biliary Tree in the Mouse Liver, related to Figure 3.**

(A) Portal veins labeled with pink metallic nanoparticle dye combined with three-dimensional DAB immunohistochemistry (CK19$^{+}$, brown) marking biliary epithelial cells. A larger view shows the accompanying distribution of bile ducts along portal veins.

(B) Portal veins labeled with pink nanoparticle dye and bile ducts labeled with green nanoparticle dye, combined with three-dimensional DAB immunohistochemistry (CK19$^{+}$, brown). The boxed region highlights a PLC structure adjacent to terminal bile duct branches.

(C) Whole-lobe overview of the liver captured by extended-depth-of-focus imaging, showing high-pressure perfusion of green dye for bile ducts and yellow dye for portal veins, visualizing the spatial relationship between biliary and vascular systems.

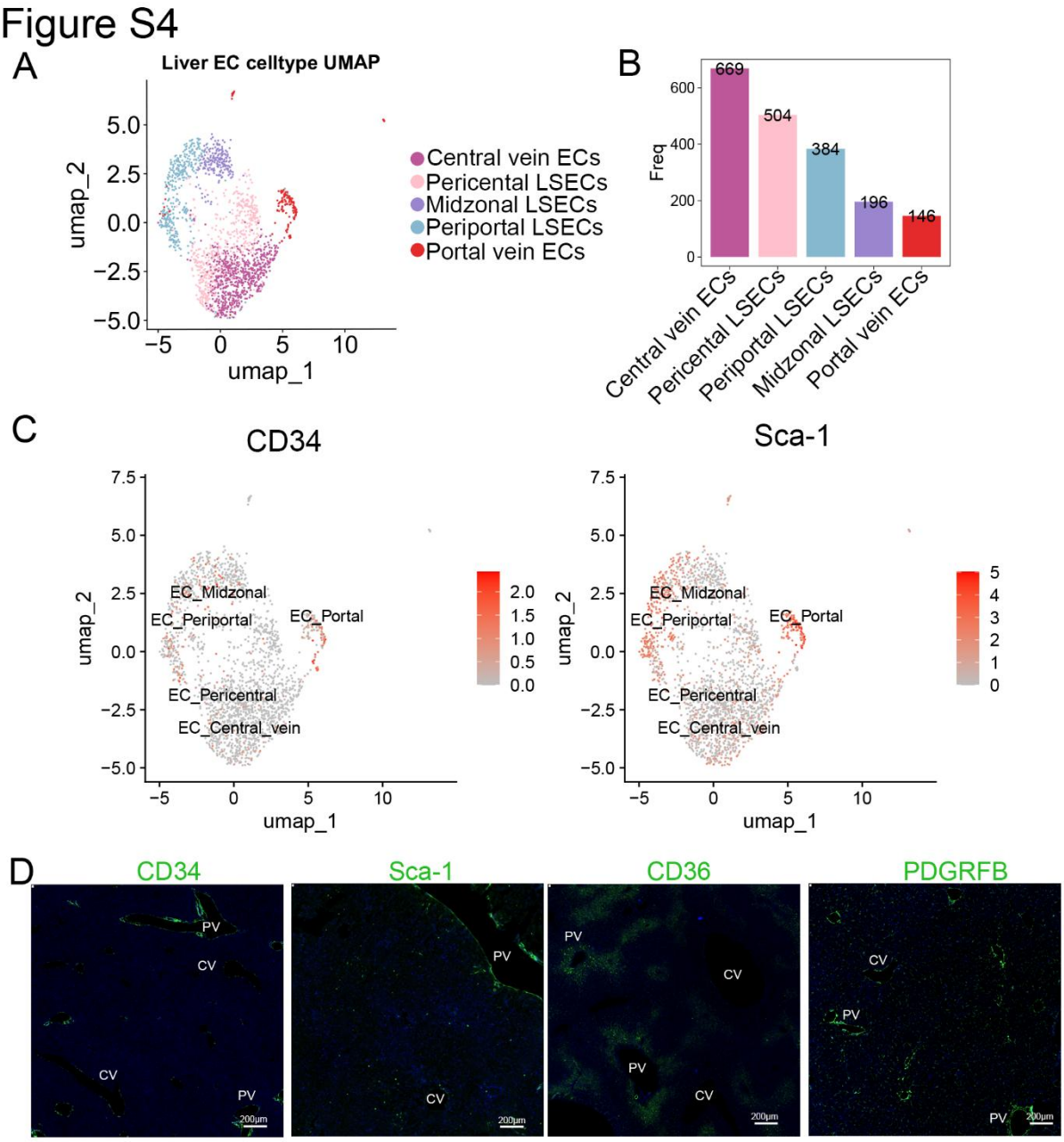


**Figure S4.Single-Cell Transcriptomic and Immunofluorescence Analysis of Endothelial Cell Subpopulations in the Mouse Liver, related to Figure4.**

(A) UMAP dimensionality reduction analysis showing five distinct endothelial cell clusters isolated from normal mouse liver after excluding non-endothelial cells. Each dot represents an individual cell.

(B) Quantification of the number of cells in the five endothelial subpopulations: Central vein ECs, Pericentral LSECs, Periportal LSECs, Midzonal LSECs, and Portal vein ECs. The results showed that Central vein ECs were the most abundant (669 cells), while Portal vein ECs were the least (146 cells). This reflects the spatial quantitative differences among liver endothelial subpopulations based on single-cell RNA sequencing clustering.

(C) UMAP-based heatmaps displaying the expression patterns of CD34 (left) and Sca-1 (right) across different liver endothelial subpopulations. Both markers were predominantly expressed in Portal vein ECs, Periportal LSECs, and Midzonal LSECs regions. The color gradient indicates expression levels, with deeper red representing higher expression.

(D) Immunofluorescence staining of CD34, Sca-1, CD36, and PDGFRB in mouse liver tissue sections. CD34 and Sca-1 were primarily localized around portal veins (PV) and adjacent vascular regions. CD36 was predominantly expressed in periportal liver sinusoidal endothelial cells, while PDGFRB showed widespread distribution in multiple intrahepatic endothelial cell populations. CV: central vein; PV: portal vein. Scale bar: 200 μm.

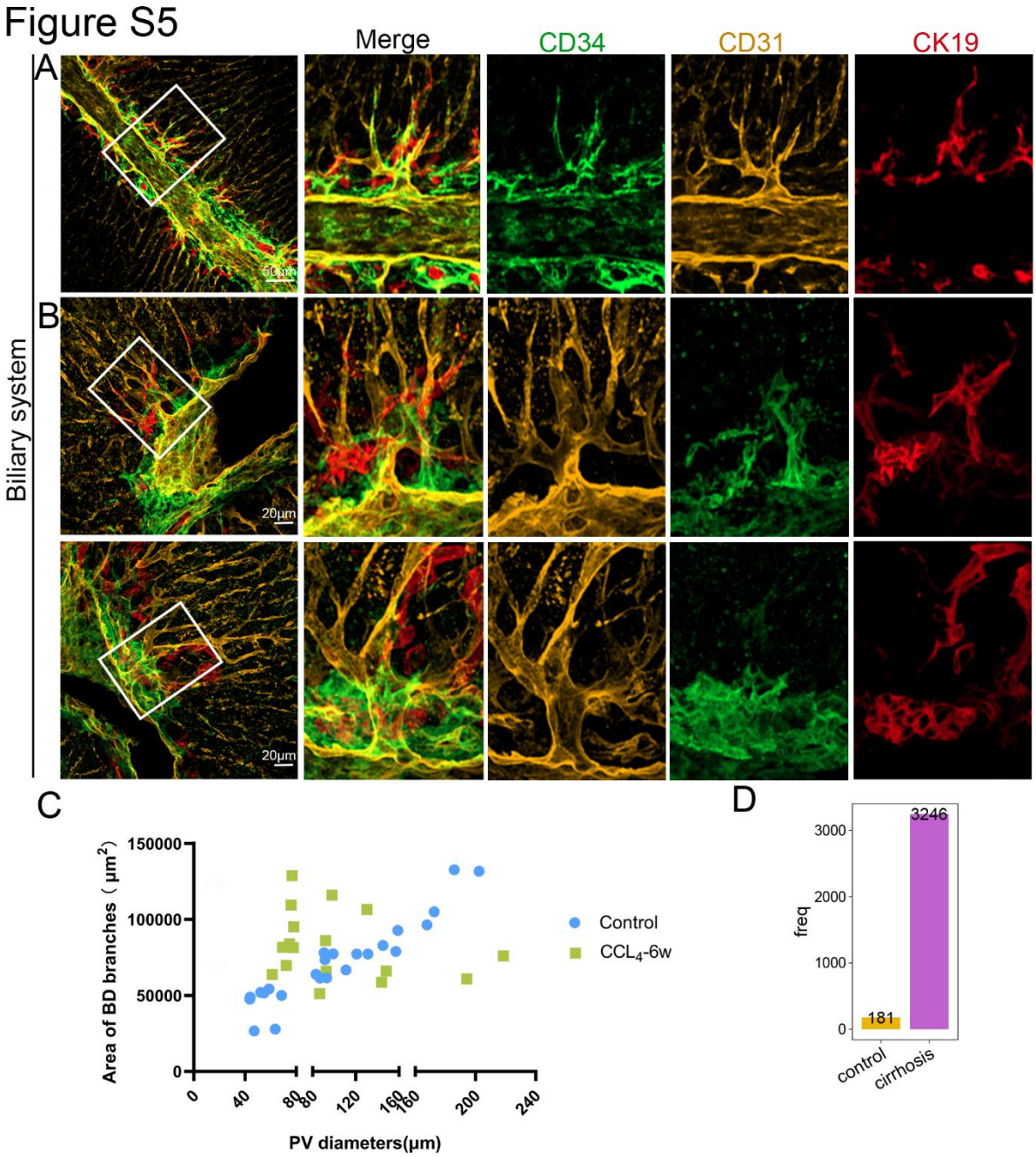


**Figure S5. Distribution of CD31⁺, Sca-1⁺, and CK19⁺ Cells and Portal Vein–Associated Bile Duct Morphology in Control and Fibrotic Mouse Livers, related to Figure5.**

(A) Multiplex immunofluorescence staining showing the distribution of CD31 (yellow), Sca-1 (green), and CK19 (red) in the liver of control mice. Scale bar: 50 μm.

(B) Higher-magnification view of multiplex immunofluorescence staining showing CD31 (yellow), Sca-1 (green), and CK19 (red) distribution in control mouse livers. Scale bar: 20 μm.

(C) Quantification of the terminal bile duct area on the surface of portal veins with different diameters in control mice. Data are presented as mean ± standard deviation (Mean ± SD). Number of portal veins: control = 20, $CCl_4$-6 weeks = 18.

(D) Quantification of $CD34^+$ $Sca\text{-}1^+$ endothelial cell subpopulations in control and fibrotic ($CCl_4$-induced) mouse livers.

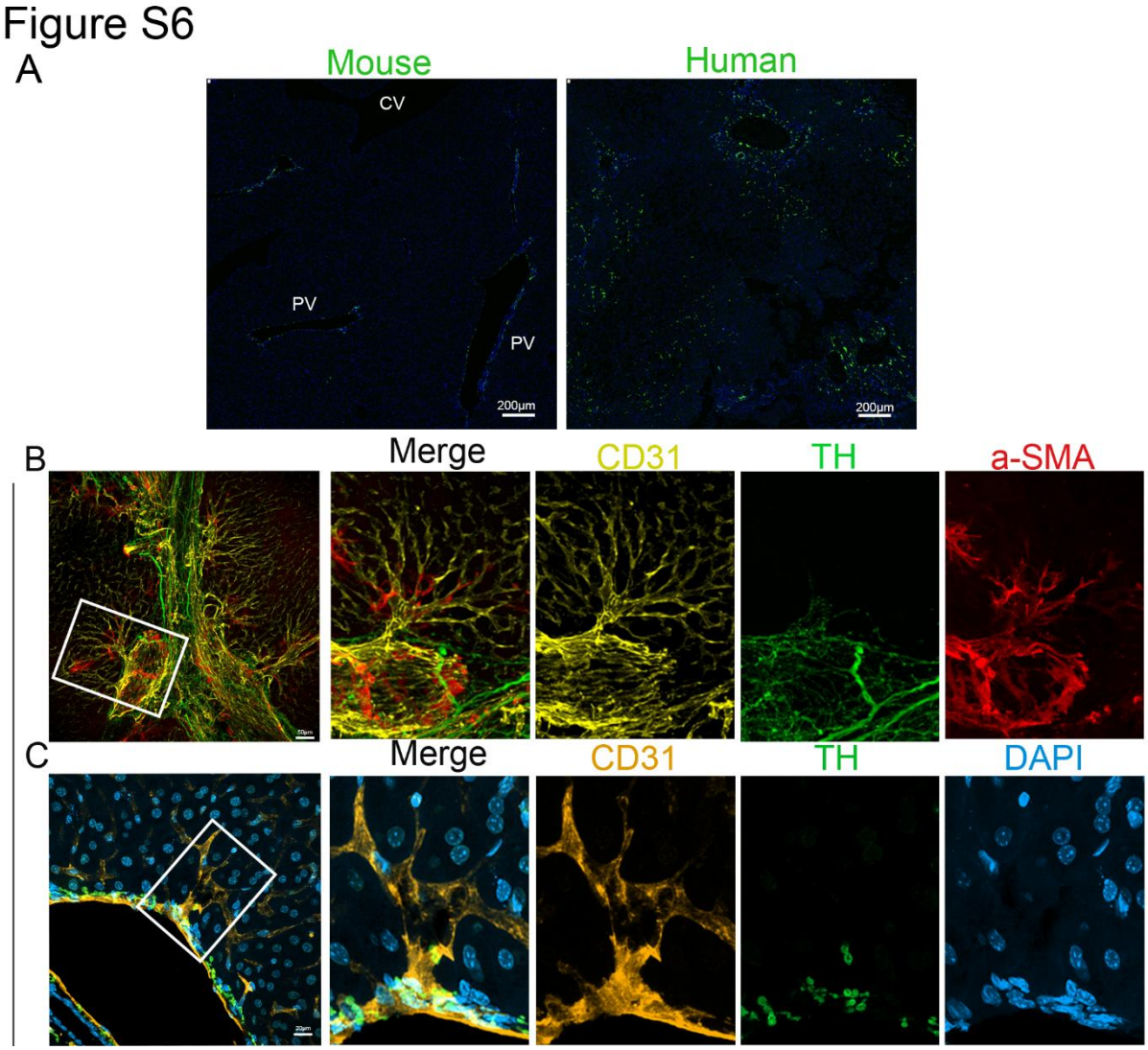


**Figure S6. Distribution of $TH^+$ Sympathetic Nerve Fibers in Mouse and Human Liver, and Their Spatial Association with Hepatic Vessels, related to Figure6.**

(A) Immunofluorescence staining showing the distribution of tyrosine hydroxylase (TH) in liver sections from both mice and humans. Scale bar: 200 μm.

(B) Multiplex immunofluorescence staining in control mouse livers showing the spatial distribution of CD31 (yellow), TH (green), and α-SMA (red). Scale bar: 50 μm.

(C) Multiplex immunofluorescence staining in control mouse livers showing the distribution of CD31 (yellow), TH (green), and DAPI (red). Scale bar: 20 μm.